UNIVERSITY OF ILLINOIS at CHICAGO
Department of Earth and Environmental Sciences
845 W. Taylor St., MC-186
Chicago, IL 60607-7059

DOE FG02-03ER63557: Final Technical Report

Reactivity of Primary Soil Minerals and Secondary Precipitates Beneath Leaking Hanford Waste Tanks

Principal Investigator: Kathryn Nagy, klnagy@uic.edu, (312) 355-3276

Goals and Objectives

The purpose of the project was to investigate rates and mechanisms of reactions between primary sediment minerals and key components of waste tank solutions that leaked into the subsurface at the Hanford Site. Results were expected to enhance understanding of processes that cause (1) changes in porosity and permeability of the sediment and resultant changes in flow paths of the contaminant plumes, (2) formation of secondary precipitates that can take up contaminants in their structures, and (3) release of mineral components that can drive redox reactions affecting dissolved contaminant mobility. Measured rates can also be used directly in reactive transport models.

Project tasks included (1) measurement of the dissolution rates of biotite mica from low to high pH and over a range of temperature relevant to the Hanford subsurface, (2) measurement of dissolution rates of quartz at high pH and in the presence of dissolved alumina, (3) measurement of the dissolution rates of plagioclase feldspar in high pH, high nitrate, high Al-bearing solutions characteristic of the BX tank farms, (4) incorporation of perrhenate in iron-oxide minerals as a function of pH, and (5) initiation of experiments to measure the formation of uranium(VI)-silicate phases under ambient conditions. Task 2 was started under a previous grant from the Environmental Management Science Program and Task 4 was partially supported by a grant to the PI from the Geosciences Program, Office of Basic Energy Sciences. Task 5 was continued under a subsequent grant from the Environmental Remediation Sciences Program, Office of Biological and Environmental Research.

Summaries of the major results and products from each task are described below.

Task 1. Dissolution of Biotite Mica as a Function of pH from 1 to 14 and Temperature from 10 to 70 degrees C

This research was conducted by Visiting Assistant Research Professor Dr. Sherry Samson with assistance by undergraduate independent study student, Danka Andjelic, both at the University of Illinois at Chicago. The work resulted in one publication and one manuscript in preparation.

Samson S. D., Nagy K. L., and Cotton, Worth B., III., 2005, Transient and steady-state dissolution of biotite at 22-25 °C in high pH, sodium, nitrate, and aluminate solutions. *Geochimica et Cosmochimica Acta* 69, 399-413.
Nagy K. L., Andjelic, D., and Samson S. D., Dissolution of biotite at pH 1-14 and 10-70°C, in preparation for submission to *Geochimica et Cosmochimica Acta*.

In the first manuscript (Samson et al., 2005) we established the dissolution rates at ambient temperature and over the basic pH range relative to the Hanford subsurface. The second manuscript in preparation is providing data that extends these rates to the full pH range and to temperatures that would be characteristic of the Hanford site both an on annual basis and as a result of heating from the radioactive wastes stored in the subsurface tanks.

Documentation of the experimental approach and results for the second manuscript are provided below.

Materials and Methods (Nagy et al., in prep.)

Preparation and Characterization of Biotite

Four batches of powdered biotite were prepared from hand samples from Bancroft, Ontario, Canada (Ward's Scientific). The biotite was cleaved, hand-picked to exclude pieces with calcium carbonate inclusions and iron oxide coatings, crushed in a shatter box with tungsten carbide grinding dishes and pucks, and sieved to obtain the 53- to 105-μm size fraction. Batch 1 was cleaned of fine particles by repeated gravity settling in acetone (Fisher, Optima). Batches 2-4 were used without further treatment. Particle size distributions (Table 1) were determined by laser diffraction of aqueous suspensions (Malvern Mastersizer 2000). The Brunauer-Emmett-Teller (BET) specific surface areas (Table 1) were measured using N_2(g) (Micromeritics TriStar 3000).
The stoichiometry, as determined from Ferrozine and electron microprobe analyses (Samson et al., 2005), was

$$(K_{1.007}Na_{0.016})(Mg_{1.609}Mn_{0.056}Fe^{2+}_{1.075}Fe^{3+}_{0.059}Ti_{0.121})(Al_{0.991}Si_{2.981})O_{10}(OH_{1.709}F_{0.283}Cl_{0.008})$$

.
Powder X-ray diffraction (XRD) (Scintag X-ray diffractometer with Cu Kα radiation, 40 kV, 20 mA, step size 0.02° 2θ, scan rate 2° 2θ min^{-1}, 2-70° 2θ) revealed only biotite.

Experiments

Sixty-eight experiments (single-*T*) were conducted with temperature (*T*) maintained at a constant value (Table 2). These experiments were designed to measure steady-state dissolution rates. Two experiments in which temperature was changed with time (multi-*T*) were carried out at pH 13: one with stepwise increases in *T* from 25°C to 70°C followed by stepwise decreases to 25°C and one with stepwise decreases from 70°C to 25°C (Table 3). These experiments were conducted to simulate the effects of in-situ temperature fluctuations in Hanford sediments beneath the radioactive waste storage tanks. All experiments were conducted in continuously stirred flow-through reactors made with materials appropriate for the range of pH and temperature conditions.

Most single-*T* reactors contained 1 g of biotite in a total volume of 41 mL (49 g biotite L^{-1}), and flow rates were typically ~ 0.5 or 1 mL min^{-1} (Table 2**)**; in the multi-*T*

experiments, reactors contained 2 g of biotite and flow rates were ~ 0.27 mL min^{-1} (Table 3). In some single-*T* experiments, flow rates were as high as 2 mL min^{-1} in the first 48 hours (see footnote, Table 2) when release rates were greatest. Influent solutions were prepared with doubly-deionized 18 MΩ-cm water (Barnstead NANOpure™ Infinity UV) titrated to the appropriate pH with HNO_3 (Fisher, TraceMetal) or NaOH (Fisher, Certified) to the following tolerances: pHs 1-4, ± 0.01 pH units; pHs 5, 12, and 13, ± 0.03; and pHs 6-11 ± 0.05. Inlet solutions for the pH 14 experiments were 1 M NaOH. Six experiments at pHs 5 and 6 were carried out in buffered solutions of 0.005 m potassium hydrogen phthalate (Fisher, Certified ACS) and twelve at pHs 8-10 were carried out in solutions buffered by 0.005 m boric acid (Fisher, Certified ACS) (Table 2).

Effluent concentrations of Si, Al, Fe, Mg, and K were analyzed by inductively coupled plasma optical emission spectrometry (ICP-OES; PerkinElmer 4300 DV) with detection limits of 3.2, 1.4, 0.8, 0.05, and 10 ppb, respectively (40, 5, 3, 0.05, and 670 ppb, respectively, in 1 M NaOH solutions). Detection limits were defined as three times the standard deviation of 50 replicate readings of blank concentrations. Rates based on sample concentrations below the analytical detection limits have been excluded from the results. An Accumet AR-15 pH meter (Fisher) and one of two electrodes were used to measure the pH of the samples. A glass combination Ag/AgCl reference electrode (Corning) calibrated with standard buffer solutions (Fisher) at pHs 1, 4, 7, and 10 and user-prepared buffer solutions at pHs 12 and 13 was used to measure the pH of all samples except those at pH 14, which were measured using a solid-state ion-sensitive field effect transistor (ISFET) pH sensor with an internal reference electrode (Ag/AgCl) and automatic temperature compensation (AccuFet, Fisher). The sensor was calibrated in millivolts (mV) in freshly prepared 1 M and 0.1 M NaOH (Fisher, Certified) solutions corresponding to pHs 14 and 13, respectively. Effluent pH was calculated from mV readings. All pH measurements were made at room temperature.

Aqueous speciation, saturation indices, and pHs at temperatures other than 25°C were calculated with The Geochemist's Workbench® 4.0.3 (GWB) (Bethke, 2002). Activity coefficients were calculated with the B-dot model subject to a maximum ionic strength of 3 molal. The thermodynamic database was modified by the substitution of Wesolowski and Palmer's (1994) data for gibbsite solubility and Al hydrolysis; the addition of phthalate species from the database *thermo_minteq_gwb4.dat*; and the addition of the minerals palygorskite ($Mg_{2.84}Al_{1.8}Si_{7.73}O_{20}(OH)_2(OH_2)_4{\cdot}4H_2O$) and kerolite ($Mg_3Si_4O_{10}(OH)_2{\cdot}H_2O$) whose solubility products (log *K*) at 25°C were computed from the free energies of formation ($\Delta G°_{f,298}$) from Stoessell (1988). The polymeric Si species $H_4(H_2SiO_4)_4^{4-}$ and $H_6(H_2SiO_4)_4^{2-}$, for which only 25°C data are available, were deleted. The species $Si_4(OH)_{18}^{-}$ for which data is available from 0 to 100°C was added and chosen to represent all polymeric Si species (Busey and Mesmer, 1977, Bickmore et al. 2001).

BET surface areas of selected reacted samples were measured using $N_2(g)$ (Micromeritics TriStar 3000) (Table 4). Particle size distributions of all reacted samples were determined by laser diffraction of aqueous suspensions (Malvern Mastersizer 2000). Powder XRD of multi-*T* sample A was carried out using a Siemens X-ray diffractometer with Cu Kα radiation, 40 kV, 25 mA, step size 0.01° 2θ, scan rate 0.12° 2θ min^{-1} (step time 5 s), 2-65° 2θ. Powder XRD of single-*T* samples was performed at Beamline 11ID-D (with flux of ~ 10^{11} photons s^{-1}) of the Advanced Photon Source, Argonne National

Laboratory. An X-ray wavelength of 0.9538 Å (13 keV) was selected with a Si (220) monochromator and scans were obtained from 2-62° 2θ at intervals of 0.02° 2θ with counting times of 1 s per step.

Calculation of Release Rates

Effluent concentrations were normalized to stoichiometric values in biotite:

$$C_{Me} = \frac{c_{Me}}{P_{Me}} \tag{3}$$

where C_{Me} is the normalized effluent concentration of *Me* [moles biotite L^{-1}], *Me* = Si, Al, Fe, Mg, K, or Ti, c_{Me} is the aqueous concentration of *Me* [moles *Me* L^{-1}], and P_{Me} is the number of moles of *Me* in one mole of biotite [moles *Me* moles $(-O_{10}(OH)_2)^{-1}$]. Steady-state release rates were calculated using

$$Rate_{Me} = \frac{qC_{Me}}{mA} \tag{4}$$

where $Rate_{Me}$ [moles biotite m^{-2} s^{-1}] is the release rate of *Me* normalized to the biotite stoichiometry and surface area, q is flow rate [L s^{-1}], m is the mass [g] of biotite in the reactor, and A is the initial biotite specific surface area [m^2 g^{-1}]. Uncertainties in elemental release rates were determined from the combined analytical uncertainties in BET surface area, flow rate, measured element concentrations, and the variability of released concentrations over intervals of time selected to approximate steady-state dissolution behavior. Although the BET surface area measurements were highly reproducible (RSDs < 1%), 5% was selected as the measurement error. Similarly, uncertainty for the measured element concentrations was defined as the standard deviation of three replicates or 10%, whichever was greater.

Rates were also calculated in an alternate format based on dissolution of a specified mass of biotite. First, the target mass of biotite, X [mg], was selected and the equivalent moles of *Me*, Me_{rel} [mol Me], were calculated using

$$Me_{rel} = \frac{(X/1000)P_{Me}}{MW_{Biotite}} \tag{5}$$

where $MW_{Biotite}$ [g mol^{-1}] is the molecular weight of the biotite. The average release rate for X mg of biotite based on the target value of Me_{rel}, $Rate_{Me,Xmg}$ [moles biotite m^{-2} s^{-1}], was then calculated based on the elapsed time, t [s], when the requisite release of *Me* was achieved:

$$Rate_{Me,Xmg} = \frac{Me_{rel}}{P_{Me}mAt} \tag{6}$$

Uncertainties in this rate format arise from three sources: analytical uncertainties in BET surface area and measured element concentrations, defined above, and the uncertainty in the mass dissolved prior to the first sample collection. The latter is the largest source of error at low pHs where initial release rates are highest.

Results (Nagy et al., in prep.)

Elemental Release Rates

At very low pHs, and particularly at 50 and 70°C, biotite dissolved so rapidly that steady states were not achieved, e.g., at pH 1, 70°C, dissolution of 5 g of biotite was nearly complete within 48 h. Rates for these experiments (all at pHs 1 and 2, and 50 and 70°C at pH 3) were obtained from slopes of the cumulative moles released over time, normalized to original surface area, and subject to a maximum percent of mass dissolved based on Mg release (9%, 7%, and 6% for pHs 1, 2, and 3, respectively). Data points prior to 5 reactor residence times, τ, where $\tau = \frac{V}{q}$, (7) were excluded to eliminate artifacts of reactor mixing. In experiment 1-70, the mass dissolved at the time of the first sample collection at 4.7 τ was already 9% so only this data point was used. Rates for all other experiments were calculated by Eqn. 4 averaged over intervals of near-constant, or nominally steady-state, rates; i.e., intervals in which rates changed little with time or else oscillated with greater variability about a constant mean value. Time intervals over which rates were averaged preceded the final variations in flow rate and ranged from 3-10 d except for two experiments with intervals of 23 and 31 d. In the latter two cases, steady-state rates were achieved relatively early, but the experiments were continued until the other experiments in the same batch of eight reached steady state at which time all reactors were shut down simultaneously. Relative standard deviations (RSD) of the elemental concentrations sampled daily in the selected time intervals are included in the reported rate uncertainties. Si rates were the most stable; the RSD for all single-*T* experiments averaged 6% and exceeded 10% in only 3 experiments. Average RSDs for other elements were greater (8% for Al, 12% for Fe, and 17% for Mg), but unlike for Si and Al, the RSDs for Fe and Mg were inversely related to concentration. Seventy-nine percent of Fe RSDs > 10% occurred where average concentrations were < 6 ppb; for Mg, 70% occurred at average concentrations < 9 ppb. In the multi-*T* experiments, steady-state rates were not achieved in every temperature interval; rates were averaged for the final three samples in each interval except the final interval at 25°C where rates were averaged for the last three samples preceding the reduction in flow rates. Release rates for Fe at 70°C should be regarded as lower limits. Within 8-21 h of reaching this *T*, yellow-brown precipitated Fe was visible in the outlet tubing; consequently, the concentrations in the sample collection tubes were less than the concentrations in the reactors. Fe release rates in reactors A and B at 70°C were 0.46 and 0.24 log units slower, respectively, than in single-*T* experiment 13-70 despite similar release rates for Si and Al (Si release rates for reactors A and B were 0.06 and 0.02 log units faster, respectively, than in experiment 13-70 while Al release rates for all three experiments were within 0.01 log units). The contaminated tubing was replaced prior to the downward steps in *T* and the replacement tubing remained free of visible precipitates. This problem did not occur in the single-*T* experiments.

Rates for 13 experiments are not reported as steady states were not achieved. In some cases, lack of a steady state was caused by problems with maintaining solution flow or stirring (8B-10, 9-25, 10B-10, 10-25, and 10-50), or with filters (5B-25, 6B-25, and 6B-25R, additional discussion in section 3.1.4). In both experiments at pH 14, 70°C (14-70 and 14-70R), stirring ceased early in the experiments, there was evidence of leakage

from the reactor fittings, and titanium was leached from the filter plates due to the combination of high pH and high temperature. In three other experiments (5-10, 6-25, and 9-50), steady-state rates were not achieved despite the absence of any apparent experimental problems.

Effects of pH

Release rates for Si and Al at 25°C (Fig. 1a) reached a minimum between pH 6 and 7, and increased in both acidic and basic solutions although rates were approximately two orders of magnitude higher at pH 1 than at pH 14. Also, despite the generally increasing trend with increasing pH in basic solutions, there is a second minimum at pH ~11. Mg release rates (Fig. 1b) trended with the Si and Al rates except they remained depressed following the second minimum. Fe release rates (Fig. 1b) were at a minimum between pHs 8 and 11 (concentrations were below detection at pHs 5-8) and increased in both acidic and basic solutions; as with Si and Al, rates were highest at acidic pH values. Rates from Samson et al. (2005) for pHs 10-14 are included for comparison.

Si release rates based on mass dissolved at 25°C for X = 15 mg and X = 30 mg (Eqn. 6; Table 5) are shown in Figure 2. Included for comparison are the 25°C Si steady-state release rates from the current study along with rates from Samson et al. (2005) for pHs 7-14 and Malmström and Banwart (1997) for pHs 2-10. Circled data points indicate experiments where < 30 mg was dissolved so time, t, was extrapolated from the available data. Rates from all three studies follow the same general pattern with pH. Rates from the current study increase from steady-state to X = 30 mg to X = 15 mg. Rates from Malmström and Banwart (1997), except at low pH, most closely correspond with rates based on mass dissolved as do the Samson et al. (2005) rates for pHs 7-9. The latter rates, as noted in the cited reference, had not reached steady state.

The same general trends with pH observed at 25°C for Si and Al were observed at 10°C (Fig. 3a,b) although the minima are defined over broader pH ranges; Si rates reach minima at pHs 7 and ~ 12 while Al rates reach minima at pHs 7-8 (below detection) and ~ 11. At 50°C (Fig. 3c), rates for both Si and Al reach minima at pHs ~ 6.5 and ~ 10, while at 70°C (Fig. 3d), rates for both were relatively insensitive to pH at pH > 6, although a first minimum is suggested at about pH 6 and a second in the range of pH 10 to 11. Fe release rates (Fig. 3a, c, and d) at 10, 50, and 70°C generally followed the same pattern as at 25°C (Fig. 3b), but the minimum is in the range of pH 7 to 10 at 10°C (concentrations were below detection at pHs 7 to 8 and 10) and pH 6 to 10 at 50 and 70°C (below detection at pH 7 to 8). Mg rates (Fig. 3a, c, and d) generally decreased with increasing pH throughout the pH range at 10, 50, and 70°C although rates seemed to level off, if not rise slightly, from pH 6 to 9. At all temperatures, dissolution was closest to stoichiometric in acidic solutions (Fig. 3a-d). Al rates were consistently higher than Si rates at pH > 8 except at pH 11.78 at 70°C (13-70, inlet solution pH 13) where the Si rate was ~ 5% faster than the Al rate.

In solutions of pH > 1, initial K release rates exceeded those of other measured elements, typically by one to two orders of magnitude. At pHs ≤ 4, subsequent rates were nearly stoichiometric, whereas at pH > 4, K release rates generally remained higher than those of other elements and were consistently higher at pHs ≥ 12. Potassium release rates followed a conventional pattern in the first 100-200 h of each experiment, i.e., rapid

initial rates followed by monotonically decreasing rates. After ~200 h, however, except in very acidic solutions, K concentrations were often erratic and highly variable; in ~20% of the experiments, concentrations in the final samples were below detection. Furthermore, analytical standard deviations for K were consistently highest of all the elements. For these reasons, we lack complete confidence in the accuracy of the rates and have not reported them.

In all experiments where Ti was analyzed except at pH 14, Ti release rates (Fig. 3a-d) were at or below stoichiometric levels indicating that titanium was not being leached from the filter plates. At inlet pH 14, the ratios of Ti release rates to Fe release rates were 3.6, 4.8, and 27 at 10, 50, and 70°C, respectively (the 25°C solution was not analyzed for Ti).

Effects of temperature

Release rates generally increased with increasing *T* at low and high pHs (Fig. 4a-d), but this pattern was less consistent in the near-neutral pH region. The differences in magnitude between rates at 10°C and 70°C were also generally greater at low and high pH, especially low pH, than in the near-neutral region. Si release rates at all pHs nearly always increased with increasing *T*, but Fe release rates, and Al and Mg rates to a lesser extent, were often nearly the same or less at 70°C than at 50°C.

In the multi-*T* experiments at pH 13, after the initial rapid release rates at the onset of the experiment, rates for reactor A declined to a steady-state at 25°C (Fig. 5a). With each subsequent increase in *T* (to 40, 55, and 70°C), there were spikes in the release rates for Si, Al, and Fe followed by declining rates. Decreasing steps in *T* (to 55, 40, and 25°C) were followed by simple declines in rates. Final rates in each temperature interval were much lower following the downward steps than in the corresponding temperature interval during the upward steps in *T*. Si and Al release rates were initially non-stoichiometric at 25 and 40°C. They began to converge at 55°C and were nearly stoichiometric at 70°C and during the following downward step to 55°C (Si rates in the latter two intervals were generally higher than Al rates by an average of 11% and 7%, respectively). This pattern was also observed in the single-*T* experiments where the differences between Si and Al release rates were smaller at 70°C than at lower temperatures (averaging < 1% for all pHs vs. 93%, 106%, and 48% at 10, 25, and 50°C, respectively, although the RSDs of the differences at all temperatures are large, ≥ 50%). The differences in Si and Al release rates were greatest at pH > 8 where, as noted in section 3.1.2, Al release rates were consistently higher with only one exception. In this pH range, differences averaged 127%, 168%, 80%, and 21% for 10, 25, 50 and 70°C, respectively. Again, RSDs of the differences were large, ≥ 45%, except at 70°C where the RSD was 15%.

After ~ 600 h of dissolution in reactor A, reactor B was added to the then-70°C water bath and following initially rapid release rates that at their peak were nearly double the peak rates observed in reactor A at 25°C (except for Mg rates which were 19% higher in reactor A), rates declined. Si release rates in reactor B were either the same as or slower than in reactor A (Fig. 5b), during the subsequent downward steps in temperature to 55 and 40°C whereas release rates for Al (Fig. 5c) and Fe (Fig. 5d) were always higher in reactor B by averages of 31% and 81%, respectively. In the experiments' final interval

at 25°C, rates for all three elements were higher in reactor B by a factor of approximately two.

Effects of buffers

There were seven sets of experiments carried out at various temperatures with buffered and unbuffered influent solutions of the same pH. A direct comparison of rates is difficult because effluent pHs differ (Table 2). For example, in one set of experiments (8B-70 and 8-70), rates were nearly identical at 70°C for buffered and unbuffered pH 8 influent solutions, although calculated effluent pHs were 7.50 and 6.76, respectively. Yet in experiments with pH 6 buffered and unbuffered influent solutions (6B-70 and 6-70), also at 70°C, calculated effluent pHs were 6.09 and 6.48, respectively, and Si and Mg rates were faster in the unbuffered solution while Al rates were slower. Fe concentrations were below the detection limit in both experiments.

Typically release rates for all elements in any experiment were rapid at the beginning and decayed to slower steady-state rates with time. The unbuffered pH 5 experiments were unique in that Fe concentrations were low initially and increased throughout the experiments. In the absence of a buffer, pH was elevated to ~ 9.8 after 1.5 h, fell ~ 3 log units within 24 h, and then gradually declined to ~ 5.5 at 240-300 h. Fe release was inversely correlated with the drift in pH. A buffered experiment at 25°C displayed conventional Fe behavior with concentrations high at the onset and then declining at the same rate as Si, Al, and Mg concentrations.

In solutions buffered with KHPhth at pH 6 and boric acid at pHs 8 and 9, Si, Al, and Mg release rates for a given experiment tended to be similar to one another and Fe release was significantly lower except at pH 6 at 10°C (6B-10) where release rates for all four elements were similar. In unbuffered solutions (except 8-70), Al release rates were noticeably lower relative to Si and Mg than in buffered solutions and were closer to Fe release rates (or below detection) than Si rates. At pH 10, there is no difference in the pattern of elemental release rates between the buffered and unbuffered solutions, but there is more variability in the data for the unbuffered solutions (the latter is true at all pH values). In unbuffered solutions with inlet pHs 6-9, pH is initially elevated and falls an average of 3 log units during the experiments, but constant pH values are achieved long before steady-state release rates and there is no discernible change in the pattern of release rates with the achievement of constant pH values. There is little pH drift in unbuffered solutions of pH 10, $\leq$ 0.4 log units.

At both pHs 5 and 6, the use of the KHPhth buffer was correlated with experimental problems encountered at 25°C. In all three cases (5B-25, 6B-25, and 6B-25R), significant back-pressure occurred due to formation of a transparent film over the filter that caused decreased flow rates. The problem was alleviated by replacing the reactor filter, but over time the film would reform and slower flow would recur. Flow rates at 50 and 70°C (6B-50 and 6B-70) were stable and despite some irregularity in the flow at 10°C (6B-10), filter replacement was not necessary and steady-state rates were achieved.

Effects of changes in flow rates

Flow rates were varied in the final 24-76 h of each single-*T* experiment. In nearly all, flow rates were reduced by 50% for the final 24-52 h; in seven, flow rates were

doubled for 24 h prior to the final reduction in flow. In 6 of the 7 experiments where flow rates were doubled, Si release rates remained the same or decreased (overall averaging a 5% decrease); in the seventh experiment (14-10) rates more than doubled. Release rates for Al, Fe, and Mg nearly always increased (by averages of 39%, 152%, and 28%, respectively), but there was much more variability than for Si rates. Decreases in flow rate most often resulted in decreases in release rates. The reduction in flow rates averaged 51% and corresponding decreases in release rates for Al, Fe, and Mg averaged 29%, 37%, and 34%, respectively. Where Si release rates decreased, the decrease averaged 17%, but in 10 experiments, the majority at pH ≥ 11, Si rates increased by an average of 28%.

In the multi-*T* experiments (Fig. 5), release rates increased when flow rates were increased and decreased when flow rates were decreased. In the 70°C interval, rates were still declining when flow was temporarily increased and after an initial spike, they continued to decrease.

Activation Energies

Dissolution rates were related to temperature through the Arrhenius expression:

$$k = A\exp\left(\frac{-E_{\exp}}{RT_K}\right) \quad (7)$$

where k [mol m^{-2} s^{-1}] is the dissolution rate, A [mol m^{-2} s^{-1}] is a pre-exponential factor, E_{exp} is the experimental activation energy, and T_K [K] is absolute temperature. Dissolution rates for pHs ≤ 6 and pHs > 11 at each T_K were calculated from linear regressions of the dissolution rate data (Fig. 6a). Experimental activation energies (Fig. 6b) were then determined from the slopes of plots of log k versus $1/T_K$ (Table 6).

Experimental activation energies varied with pH, declining with increasing pH at pH ≤ 6 and increasing with increasing pH at pH ≥ 11. At lower pH, E_{exp} were calculated both including and excluding the 10°C data, the slope of which differs from that of other temperatures. At higher pH, the 70°C data has been omitted as only two data points are available in this region.

Saturation States

Thermodynamic information is not available to calculate saturation indices with respect to biotite, but GWB calculations provided indices with respect to phlogopite, the pure-Mg analogue, $KMg_3AlSi_3O_{10}(OH)_2$, and annite, the pure-Fe analogue, $KFe_3AlSi_3O_{10}(OH)_2$. All solutions at all pHs and temperatures were undersaturated with respect to both phases. Biotite saturation indices were estimated by interpolating between the two analogues based on stoichiometric values for Fe and Mg in the biotite (Fig. 7). Ionic strength did not exceed 0.212 m except for the three experiments at pH 14 where it ranged from 1.285 to 2.025 m.

In regard to secondary phases judged kinetically most likely to precipitate, all solutions at all pHs and temperatures were undersaturated with respect to amorphous silica, $SiO_{2(am)}$, (except experiment 1-70) and kaolinite, $Al_2Si_2O_5(OH)_4$. Solutions at pHs 13 and 14 were either supersaturated with respect to brucite, $Mg(OH)_2$, (electronic annex, EA-1) or Mg was below detection. Eight solutions between pHs 4 and 9 were supersaturated with respect to gibbsite, $Al(OH)_3$; in eight solutions, Al was below detection. Between pHs 6 and 10, Fe was below detection in 12 solutions and two were

supersaturated with respect to ferrihydrite ($Fe(OH)_{3(ppd)}$ in GWB notation); experiment 3-70 was also supersaturated with respect to ferrihydrite. Where Fe was detectable in solution, all solutions at all pHs and temperatures were supersaturated with respect to hematite, α-Fe_2O_3, and goethite, α-FeOOH, except at pH 1 at 10, 25, and 50°C (1-10, 1-25, and 1-50).

With respect to other secondary phases, several solutions at pHs 12-14 were supersaturated with respect to antigorite, $Mg_{24}Si_{17}O_{42.5}(OH)_{31}$, and/or chrysotile, $Mg_3Si_2O_5(OH)_4$. The SiO_2 polymorphs quartz, chalcedony, tridymite, or cristobalite were supersaturated in most pH 1 and pH 2 solutions; magnesioferrite, $MgFe_2O_4$**,** was supersaturated in 11 high pH solutions**,** and the solution in experiment 6B-50 was supersaturated with respect to diaspore. Thirty-two solutions were analyzed for Ti and 15 had detectable concentrations; rutile (TiO_2) was supersaturated in all 15 and 12 were also supersaturated with respect to anatase (TiO_2). Finally, nearly 40% of the solutions between pHs 1 and 10 were supersaturated with respect to nontronite, $(K, Na)_{0\text{-}0.33}(Mg)_{0\text{-}0.165}Fe_2Al_{0.33}Si_{3.67}O_{10}(OH)_2$.

Solutions in the pH 13 multi-*T* experiments were supersaturated with respect to hematite, goethite, and brucite at all temperatures (EA-1). Chrysotile and antigorite were supersaturated in all solutions except reactor A at the conclusion of the experiment at 25°C and in reactor B at 40°C. Magnesioferrite was supersaturated in all solutions except reactor A at 40 and 25°C during the downward steps in temperature.

Thermodynamic information for the minerals palygorskite and kerolite was available only at 25°C so saturation indices were calculated only for experiments at this temperature. All solutions, single-*T* and multi-*T*, at all pHs at 25°C were undersaturated with indices ranging from -22 to -59 for palygorskite and -10 to -47 for kerolite.

Solids Characterization

Post-experiment BET surface area analysis was performed on five samples selected to represent a range of pH, *T*, and percent of mass dissolved (Table 4). Specific surface area increased for all samples, but there was no correlation between changes in surface area and the percent of the original mass of biotite dissolved. Nor was there any correlation with experimental temperature, pH, or total hours of dissolution. There was a good correlation between BET surface area and mean particle-size diameter for the four batches of unreacted biotite, and we had hoped to use changes in mean particle size as a proxy for changes in surface area, but a correlation for reacted biotite wasn't supported by the available data. Release rates were calculated based on the original surface area measurements for each batch of biotite.

One multi-*T* sample (Fig. 8; reactor A) and eight single-*T* samples (Fig. 9), selected to represent a range of pH, *T*, percent of mass dissolved, and supersaturation with respect to secondary phases, were analyzed by X-ray diffraction. Patterns were interpreted with JADE search/match software (Materials Data, 2005) using reference patterns in the Powder Diffraction File (ICDD, 2005). The only phase reported as a match for any of the patterns was fluorannite, ($KFe_3AlSi_3O_{10}F_2$, PDF card #53-1188), but a biotite 1M pattern ($KMg_2Al_2,Si_3O_{11}(OH)$, PDF card #76-884) is also a very close match and includes all peaks common to all of the patterns whereas the fluorannite pattern does not. A peak at 3.04 Å (29°2θ), in the pH 4, 70°C, pattern likely is from potassium nitrate, KNO_3. We attempted to match the other unidentified peaks with a manual search of the

Hanawalt index (ICDD, 2001), but were unable to identify any other secondary phases, including those for which supersaturation was indicated by GWB calculations. An unidentified peak at 2.81 Å in the pH 12, 70°C, pattern is close to the primary siderite peak at 2.795 Å; the saturation index with respect to this phase, however, is -20.

With respect to iron (hydr)oxide phases, the primary peak (104) for hematite is located at 2.69 Å (33°2θ), coincident with a biotite peak located at 2.70 Å which is present in all of the patterns except pH 14. The second and third most intense hematite peaks, (116) at 1.69 Å (54°2θ) and (110) at 2.51 Å (36°2θ), would be obscured partially and completely, respectively, by biotite peaks at 1.675 Å and 2.51 Å. The primary peak for 6-line ferrihydrite, (110) at 2.5 Å (36°2θ), would likewise be obscured by the biotite peak, and the two next most intense peaks, (112) at 2.21 Å (41°2θ), and (113) at 1.96 Å (46°2θ), are absent from all patterns. The primary goethite peak, (100) at 4.183 Å (21°2θ), is also absent from all patterns.

The pH 14, 50°C, pattern (Fig. 10) indicates random interstratification as evidenced by the (001) peak shift from 10 Å to 12 Å and the diffraction band at ~19°2θ. This is consistent with previous observations of the formation of vermiculite layers at irregular intervals within altered biotite (Banfield and Eggleton, 1988; Ferrow et al., 1999; Jeong and Kim, 2003; Kogure and Murakami, 1996) and of accelerated vermiculitization in high sodium solutions, 1 M in this instance (Malmström and Banwart, 1997; Samson et al., 2005).

BET surface areas were measured for two of the X-rayed samples: pH 12, 70°C, and pH 1, 10°C. Despite a dramatic difference in the percent of the original mass dissolved, 7% vs. 58%, there is little difference in the XRD patterns suggesting the biotite structure was unaltered as the particles dissolved.

Table 1. Unreacted biotite.

	Batch 1	**Batch 2**	**Batch 3**	**Batch 4**
Particle Size (μm)				
≤ 52.556	35.8%	47.5%	49.8%	55.3%
> 52.556 ≤ 105.1121	40.5%	34.5%	34.0%	31.3%
> 105.1121	23.7%	18.0%	16.2%	13.4%
Mean	72.967	61.895	59.220	53.601
BET Surface Area ($m^2 g^{-1}$)	3.2486	5.1090	4.6226	5.4213
Error	± 0.0086	± 0.0077	± 0.0050	± 0.0016

Table 2. Single-*T* experiments summary.

Exp. ID	Temp (C)	Inlet pH	Buffer	Biotite (g)	Biotite Batch	Flow Rate (mL min^{-1})[a]	Time (h)	% Diss[b]	Meas. pH[c]	Calc. pH[d]	log $Rate_{Me}$ (moles biotite m^{-2} s^{-1})[e]				
											Si	Al	Fe	Mg	K
1-10	10	1		4.00359	3	1.042±0.068	175	58.18	1.025	1.024	$-9.87^{+0.05}_{-0.05}$	$-9.62^{+0.05}_{-0.05}$	$-9.58^{+0.05}_{-0.05}$	$-9.64^{+0.05}_{-0.05}$	$-9.67^{+0.05}_{-0.05}$
2-10	10	2		4.01029	3	0.514±0.039	1367	30.21	2.037	2.037	$-10.36^{+0.05}_{-0.05}$	$-9.97^{+0.05}_{-0.05}$	$-9.93^{+0.05}_{-0.05}$	$-10.05^{+0.05}_{-0.05}$	$-10.03^{+0.05}_{-0.05}$
3-10	10	3		2.00376	3	0.447±0.044	1367	13.76	3.059	3.061	$-11.18^{+0.05}_{-0.06}$	$-10.99^{+0.06}_{-0.08}$	$-10.98^{+0.06}_{-0.07}$	$-11.00^{+0.05}_{-0.06}$	$-11.12^{+0.09}_{-0.11}$
4-10	10	4		1.00549	2	0.531±0.036	1367	4.91	4.088	4.089	$-11.62^{+0.06}_{-0.07}$	$-11.77^{+0.06}_{-0.07}$	$-11.53^{+0.05}_{-0.06}$	$-11.61^{+0.06}_{-0.06}$	$-11.55^{+0.12}_{-0.17}$
5-10	10	5		1.00668	2	0.533±0.026	1367	2.49	5.608	5.676	NR[f]	NR[f]	NR[f]	NR[f]	NR[f]
6B-10	10	6	KHPhth	1.00295	2	0.492±0.018	2041	1.94	6.031	6.027	$-12.31^{+0.13}_{-0.19}$	$-12.27^{+0.11}_{-0.15}$	$-12.26^{+0.19}_{-0.34}$	$-12.34^{+0.15}_{-0.23}$	NA[h]
6-10	10	6		0.99451	2	0.468±0.006	2064	2.42	6.210	6.287	$-12.41^{+0.05}_{-0.06}$	BD[g]	$-13.38^{+0.26}_{-0.70}$	$-12.29^{+0.07}_{-0.08}$	$-12.25^{+0.35}_{BD}$
8B-10	10	8	H_3BO_3	1.00500	2	0.458±0.023	2041	2.11	7.939	8.060	NR[f]	NR[f]	NR[f]	NR[f]	NR[f]
9-10	10	9		1.00057	2	0.464±0.009	2064	2.80	7.027	7.120	$-12.65^{+0.06}_{-0.07}$	BD[g]	BD[g]	$-12.62^{+0.12}_{-0.16}$	BD[g]
9B-10	10	9	H_3BO_3	1.00393	2	0.452±0.015	2048	3.51	8.991	9.115	$-12.35^{+0.05}_{-0.06}$	$-12.32^{+0.05}_{-0.06}$	$-13.07^{+0.06}_{-0.07}$	$-12.56^{+0.05}_{-0.06}$	$-11.85^{+0.07}_{-0.08}$
10-10	10	10		1.00007	2	0.397±0.017	2402	3.03	9.475	9.971	$-12.54^{+0.06}_{-0.07}$	$-12.49^{+0.07}_{-0.08}$	BD[g]	$-12.76^{+0.10}_{-0.12}$	$-12.34^{+0.45}_{BD}$
10B-10	10	10	H_3BO_3	0.99232	2	0.469±0.017	1704	4.15	9.918	10.071	NR[f]	NR[f]	NR[f]	NR[f]	NR[f]
11-10	10	11		0.99819	2	0.446±0.007	2064	3.35	10.848	11.379	$-12.68^{+0.05}_{-0.05}$	$-12.53^{+0.06}_{-0.07}$	$-13.66^{+0.22}_{-0.45}$	$-13.50^{+0.10}_{-0.13}$	BD[g]
12-10	10	12		0.99840	2	0.462±0.008	2064	2.82	11.969	12.502	$-12.80^{+0.07}_{-0.08}$	$-12.43^{+0.06}_{-0.07}$	$-13.00^{+0.05}_{-0.05}$	BD[g]	$-12.22^{+0.17}_{-0.30}$
13-10	10	13		1.00069	2	0.465±0.010	2064	2.99	12.865	13.399	$-12.52^{+0.05}_{-0.05}$	$-11.92^{+0.05}_{-0.05}$	$-12.41^{+0.05}_{-0.05}$	BD[g]	$-11.12^{+0.10}_{-0.13}$
14-10	10	14		1.00351	2	0.516±0.032	1396	3.51	14.094	14.621	$-12.13^{+0.06}_{-0.07}$	$-11.56^{+0.05}_{-0.06}$	$-12.01^{+0.05}_{-0.06}$	BD[g]	BD[g]
1-25	25	1		1.00136	1	0.739±0.193	504	101.06	1.048	1.048	$-9.29^{+0.05}_{-0.05}$	$-9.02^{+0.05}_{-0.05}$	$-8.98^{+0.05}_{-0.05}$	$-9.08^{+0.05}_{-0.05}$	$-9.05^{+0.05}_{-0.05}$
2-25	25	2		0.99808	1	0.762±0.231	365	37.26	2.045	2.045	$-9.63^{+0.05}_{-0.05}$	$-9.26^{+0.05}_{-0.05}$	$-9.16^{+0.05}_{-0.05}$	$-9.37^{+0.05}_{-0.05}$	$-9.28^{+0.05}_{-0.05}$
3-25	25	3		1.00544	1	0.995±0.023	504	11.99	3.106	3.106	$-10.54^{+0.05}_{-0.05}$	$-10.53^{+0.05}_{-0.06}$	$-10.42^{+0.05}_{-0.05}$	$-10.49^{+0.05}_{-0.05}$	$-10.72^{+0.07}_{-0.09}$
4-25	25	4		1.00533	1	0.954±0.020	504	4.52	4.247	4.247	$-11.06^{+0.06}_{-0.06}$	$-11.37^{+0.05}_{-0.06}$	$-11.10^{+0.05}_{-0.06}$	$-11.23^{+0.06}_{-0.07}$	BD[g]
5-25R	25	5		0.99833	4	0.962±0.003	2088	4.06	5.232	5.232	$-12.16^{+0.05}_{-0.06}$	BD[g]	$-12.00^{+0.08}_{-0.10}$	$-12.23^{+0.10}_{-0.13}$	$-11.18^{+0.21}_{-0.40}$
5B-25	25	5	KHPhth	0.99852	4	0.533±0.027	1751	3.53	5.012	5.012	NR[f]	NR[f]	NR[f]	NR[f]	NR[f]
6-25	25	6		0.99389	1	0.974±0.022	504	2.41	6.341	6.341	NR[f]	NR[f]	NR[f]	NR[f]	NR[f]
6B-25	25	6	KHPhth	0.99677	1	0.518±0.151	743	1.91	6.088	6.088	NR[f]	NR[f]	NR[f]	NR[f]	NR[f]
6B-25R	25	6	KHPhth	1.00114	4	0.932±0.027	2088	1.73	6.006	6.006	NR[f]	NR[f]	NR[f]	NR[f]	NR[f]

Exp. ID	Temp (C)	Inlet pH	Buffer	Biotite (g)	Biotite Batch	Flow Rate (mL min^{-1})[a]	Time (h)	% Diss[b]	Meas. pH[c]	Calc. pH[d]	log $Rate_{Me}$ (moles biotite m^{-2} s^{-1})[e]				
											Si	Al	Fe	Mg	K
8-25	25	8		1.00039	4	0.919±0.011	2087	2.71	6.695	6.695	$-12.73^{+0.06}_{-0.07}$	BD[g]	BD[g]	$-12.62^{+0.19}_{-0.33}$	$-11.90^{+0.29}_{-1.15}$
8B-25R	25	8	H_3BO_3	1.00197	4	0.926±0.015	2087	2.80	7.942	7.942	$-12.46^{+0.05}_{-0.06}$	$-12.50^{+0.09}_{-0.11}$	BD[g]	$-12.46^{+0.09}_{-0.11}$	BD[g]
9-25	25	9		0.99333	4	0.929±0.003	2087	2.86	7.354	7.354	NR[f]	NR[f]	NR[f]	NR[f]	NR[f]
9B-25R	25	9	H_3BO_3	1.00454	4	0.948±0.004	2087	3.85	8.992	8.992	$-12.21^{+0.05}_{-0.06}$	$-12.15^{+0.06}_{-0.07}$	$-12.90^{+0.08}_{-0.10}$	$-12.22^{+0.05}_{-0.06}$	$-11.68^{+0.36}_{BD}$
10-25	25	10		1.00154	4	0.962±0.003	2087	3.17	9.670	9.670	NR[f]	NR[f]	NR[f]	NR[f]	NR[f]
10B-25	25	10	H_3BO_3	1.00334	1	0.923±0.051	743	3.10	10.016	10.016	$-11.98^{+0.05}_{-0.06}$	$-11.87^{+0.05}_{-0.06}$	$-12.94^{+0.06}_{-0.07}$	$-12.03^{+0.05}_{-0.06}$	$-11.41^{+0.09}_{-0.11}$
11-25	25	11		0.99511	1	0.922±0.021	743	2.05	11.004	11.004	$-12.45^{+0.05}_{-0.06}$	$-12.19^{+0.05}_{-0.05}$	$-12.95^{+0.07}_{-0.09}$	$-12.59^{+0.05}_{-0.06}$	BD[g]
12-25	25	12		1.00532	1	0.851±0.112	743	2.04	11.970	11.970	$-12.18^{+0.05}_{-0.05}$	$-11.70^{+0.05}_{-0.05}$	$-12.32^{+0.05}_{-0.05}$	$-12.89^{+0.15}_{-0.23}$	$-10.83^{+0.06}_{-0.07}$
13-25	25	13		0.99889	1	0.951±0.019	503	3.11	12.948	12.948	$-11.82^{+0.05}_{-0.06}$	$-11.29^{+0.08}_{-0.10}$	$-11.57^{+0.05}_{-0.06}$	$-12.74^{+0.23}_{-0.51}$	$-10.34^{+0.05}_{-0.06}$
14-25	25	14		0.99888	1	0.990±0.024	503	3.95	13.909	13.909	$-11.53^{+0.06}_{-0.07}$	$-10.79^{+0.05}_{-0.06}$	$-11.13^{+0.05}_{-0.06}$	BD[g]	$-9.95^{+0.08}_{-0.09}$
1-50	50	1		1.00118	1	0.998±0.013	506	93.47	0.962	0.966	$-8.63^{+0.05}_{-0.05}$	$-8.42^{+0.05}_{-0.05}$	$-8.40^{+0.05}_{-0.05}$	$-8.47^{+0.05}_{-0.05}$	$-8.45^{+0.05}_{-0.05}$
2-50	50	2		1.00454	1	1.042±0.027	506	93.19	2.073	2.073	$-9.23^{+0.05}_{-0.05}$	$-8.94^{+0.05}_{-0.05}$	$-8.86^{+0.05}_{-0.05}$	$-9.00^{+0.05}_{-0.05}$	$-8.99^{+0.05}_{-0.05}$
3-50R	50	3		4.00140	3	0.944±0.023	1753	37.54	3.173	3.166	$-9.98^{+0.05}_{-0.05}$	$-9.97^{+0.05}_{-0.05}$	$-9.82^{+0.05}_{-0.05}$	$-9.93^{+0.05}_{-0.05}$	$-9.85^{+0.05}_{-0.05}$
4-50R	50	4		1.49974	2	0.950±0.019	1753	13.25	4.132	4.126	$-11.21^{+0.05}_{-0.06}$	$-11.33^{+0.05}_{-0.06}$	$-11.19^{+0.05}_{-0.06}$	$-11.25^{+0.05}_{-0.06}$	$-11.16^{+0.14}_{-0.20}$
5-50R	50	5		1.00137	2	0.985±0.027	1753	5.99	5.162	5.156	$-11.97^{+0.05}_{-0.05}$	BD[g]	$-12.35^{+0.05}_{-0.05}$	$-12.05^{+0.05}_{-0.05}$	BD[g]
6B-50	50	6	KHPhth	1.00255	1	0.961±0.016	769	2.62	6.091	6.094	$-11.83^{+0.06}_{-0.07}$	$-11.80^{+0.07}_{-0.08}$	$-12.54^{+0.07}_{-0.08}$	$-11.74^{+0.05}_{-0.06}$	NA[h]
6-50R	50	6		1.00022	2	0.976±0.033	1752	5.06	6.089	6.039	$-12.09^{+0.05}_{-0.06}$	BD[g]	BD[g]	$-12.13^{+0.07}_{-0.08}$	BD[g]
8B-50	50	8	H_3BO_3	1.00126	1	0.985±0.011	769	4.12	8.021	7.801	$-11.61^{+0.06}_{-0.06}$	$-11.56^{+0.06}_{-0.07}$	BD[g]	$-11.57^{+0.07}_{-0.08}$	$-10.45^{+0.16}_{-0.26}$
8-50	50	8		1.00110	2	0.972±0.025	1752	4.45	6.560	6.481	$-12.26^{+0.05}_{-0.05}$	BD[g]	BD[g]	$-12.46^{+0.11}_{-0.15}$	$-11.66^{+0.10}_{-0.12}$
9-50	50	9		0.99783	2	0.893±0.043	1752	4.97	6.889	6.771	NR[f]	NR[f]	NR[f]	NR[f]	NR[f]
9B-50	50	9	H_3BO_3	1.00282	1	1.004±0.013	769	3.93	9.068	8.841	$-11.69^{+0.05}_{-0.05}$	$-11.61^{+0.05}_{-0.06}$	$-12.53^{+0.10}_{-0.13}$	$-11.83^{+0.07}_{-0.08}$	BD[g]
10-50	50	10		1.00087	2	0.931±0.047	1752	5.48	9.291	8.572	NR[f]	NR[f]	NR[f]	NR[f]	NR[f]
10B-50	50	10	H_3BO_3	1.00311	1	0.985±0.053	769	3.45	10.023	9.700	$-11.73^{+0.05}_{-0.06}$	$-11.62^{+0.05}_{-0.05}$	$-12.33^{+0.07}_{-0.09}$	$-11.76^{+0.07}_{-0.09}$	$-11.19^{+0.07}_{-0.08}$
11-50	50	11		0.99900	1	0.988±0.016	751	3.03	10.920	10.188	$-11.95^{+0.05}_{-0.06}$	$-11.82^{+0.05}_{-0.06}$	$-12.63^{+0.09}_{-0.11}$	$-12.54^{+0.06}_{-0.07}$	$-11.20^{+0.22}_{-0.47}$
12-50	50	12		0.99449	1	0.971±0.017	769	4.23	11.954	11.219	$-11.91^{+0.05}_{-0.05}$	$-11.53^{+0.05}_{-0.05}$	$-12.20^{+0.05}_{-0.06}$	$-12.66^{+0.07}_{-0.09}$	$-10.69^{+0.05}_{-0.06}$
13-50R	50	13		1.00174	1	0.971±0.010	769	5.63	12.964	12.227	$-11.71^{+0.05}_{-0.06}$	$-11.21^{+0.05}_{-0.06}$	$-11.52^{+0.05}_{-0.05}$	$-13.24^{+0.19}_{-0.35}$	$-10.36^{+0.06}_{-0.07}$

Exp. ID	Temp (C)	Inlet pH	Buffer	Biotite (g)	Biotite Batch	Flow Rate (mL min^{-1})[a]	Time (h)	% Diss[b]	Meas. pH[c]	Calc. pH[d]	log $Rate_{Me}$ (moles biotite m^{-2} s^{-1})[e]				
											Si	Al	Fe	Mg	K
14-50R	50	14		1.00018	1	1.000±0.009	769	5.57	13.901	13.169	$-11.37^{+0.08}_{-0.10}$	$-11.23^{+0.22}_{-0.46}$	$-11.27^{+0.07}_{-0.08}$	$-12.11^{+0.09}_{-0.11}$	$-10.29^{+0.20}_{-0.37}$
1-70	70	1		5.01032	3	0.983±0.090	600	93.93	1.069	1.079	$-8.37^{+0.05}_{-0.05}$	$-8.04^{+0.05}_{-0.05}$	$-8.06^{+0.05}_{-0.05}$	$-8.11^{+0.05}_{-0.05}$	$-7.85^{+0.05}_{-0.05}$
2-70	70	2		5.00333	3	0.976±0.038	600	89.05	2.154	2.148	$-9.14^{+0.05}_{-0.05}$	$-9.01^{+0.05}_{-0.05}$	$-8.98^{+0.05}_{-0.05}$	$-9.08^{+0.05}_{-0.05}$	$-9.08^{+0.05}_{-0.05}$
3-70	70	3		4.00305	3	1.005±0.024	600	29.34	3.214	3.196	$-9.89^{+0.05}_{-0.05}$	$-10.00^{+0.05}_{-0.05}$	$-9.79^{+0.05}_{-0.05}$	$-9.84^{+0.05}_{-0.05}$	$-9.78^{+0.05}_{-0.05}$
4-70	70	4		1.99956	2	0.980±0.049	600	8.26	4.227	4.210	$-11.06^{+0.05}_{-0.06}$	$-11.40^{+0.05}_{-0.06}$	$-11.04^{+0.05}_{-0.06}$	$-11.03^{+0.06}_{-0.07}$	$-10.86^{+0.08}_{-0.10}$
5-70	70	5		1.00761	2	1.028±0.031	600	7.08	5.467	5.450	$-11.28^{+0.05}_{-0.05}$	BD[g]	$-12.90^{+0.10}_{-0.14}$	$-11.24^{+0.05}_{-0.05}$	$-11.18^{+0.09}_{-0.11}$
6B-70	70	6	KHPhth	1.00033	2	0.944±0.029	600	3.30	6.086	6.089	$-11.96^{+0.05}_{-0.06}$	$-11.78^{+0.05}_{-0.06}$	BD[g]	$-11.96^{+0.05}_{-0.05}$	NA[h]
6-70	70	6		1.00180	2	0.986±0.023	600	5.54	6.637	6.480	$-11.51^{+0.05}_{-0.06}$	$-12.33^{+0.11}_{-0.14}$	BD[g]	$-11.50^{+0.13}_{-0.19}$	$-10.77^{+0.15}_{-0.23}$
8B-70	70	8	H_3BO_3	1.00026	2	0.981±0.034	601	5.36	7.887	7.498	$-11.44^{+0.05}_{-0.05}$	$-11.45^{+0.05}_{-0.05}$	BD[g]	$-11.47^{+0.05}_{-0.05}$	$-11.22^{+0.05}_{-0.06}$
8-70	70	8		0.99186	2	0.985±0.047	600	5.62	7.094	6.757	$-11.44^{+0.06}_{-0.07}$	$-11.54^{+0.05}_{-0.06}$	BD[g]	$-11.45^{+0.12}_{-0.16}$	$-10.74^{+0.18}_{-0.31}$
9B-70	70	9	H_3BO_3	0.99970	2	0.984±0.033	600	4.93	8.972	8.571	$-11.68^{+0.05}_{-0.05}$	$-11.52^{+0.05}_{-0.06}$	$-13.17^{+0.11}_{-0.16}$	$-11.73^{+0.05}_{-0.05}$	BD[g]
10B-70	70	10	H_3BO_3	1.00026	2	1.005±0.032	600	4.89	9.892	9.360	$-11.67^{+0.05}_{-0.06}$	$-11.58^{+0.05}_{-0.06}$	BD[g]	$-11.78^{+0.06}_{-0.07}$	$-10.26^{+0.37}_{BD}$
11-70	70	11		1.00021	2	0.949±0.029	600	4.39	10.747	9.544	$-11.74^{+0.05}_{-0.06}$	$-11.65^{+0.05}_{-0.05}$	$-13.36^{+0.15}_{-0.24}$	$-12.64^{+0.05}_{-0.05}$	$-11.45^{+0.14}_{-0.21}$
12-70	70	12		0.99964	2	1.007±0.043	600	6.91	11.947	10.738	$-11.72^{+0.05}_{-0.05}$	$-11.66^{+0.06}_{-0.07}$	$-12.41^{+0.05}_{-0.06}$	$-13.18^{+0.10}_{-0.12}$	$-10.88^{+0.05}_{-0.05}$
13-70	70	13		0.99951	2	0.984±0.040	600	9.17	12.993	11.780	$-11.50^{+0.06}_{-0.07}$	$-11.52^{+0.08}_{-0.09}$	$-11.59^{+0.07}_{-0.09}$	$-12.88^{+0.10}_{-0.13}$	$-10.33^{+0.05}_{-0.06}$
14-70	70	14		1.00011	2	1.093±0.159	600	12.36	13.976	12.771	NR[f]	NR[f]	NR[f]	NR[f]	NR[f]
14-70R	70	14		2.00210	2	1.010±0.039	600	5.26	13.994	12.790	NR[f]	NR[f]	NR[f]	NR[f]	NR[f]

[a]Flow rates shown represent average rates for the duration of the experiments with the following exceptions. In most experiments (all except 6-10 through 13-10 and 5-25R through 9B-25R), flow rates were approximately doubled in the first 48 h and in nearly all experiments, flow rates were varied in the final 24-76 h to ascertain the effect of flow rate on release rates. In these instances, the first 48 h and the final 24-76 h have been excluded from calculations of average flow rates. The error is one standard deviation.

[b]Percent of mass dissolved is based on Si release except for pH 1-3 samples which are based on Mg release (except 1-25, 1-50, and 2-50 where Si was greater than Mg release).

[c]Samples from experiments conducted at 10, 50, and 70°C were allowed to equilibrate to room temperature (approximately 23°C) before pH was measured.

[d]The pH measured at room temperature was used as input to the geochemical modeling program The Geochemist's Workbench® 4.0.3 which was used to calculate the equivalent pH at the experimental temperature.

[e]Uncertainties in the rates were determined by error propagation based on uncertainties in flow rate, BET surface area (5%), ICP-OES analysis (standard deviation of 3 replicate readings or 10%, whichever was greater), and average concentration (standard deviation of the readings comprising the average). Where the lower limit is designated "BD", after error propagation the final rate was negative.

[f]NR: rates not reported, did not reach steady state or other experimental problems.

[g]BD: effluent concentration was below the analytical detection limit.

[h]NA: K not analyzed for dissolution as buffer solution is 0.005 m K.

Table 3. pH 13, multi-*T* experiments summary.

Temp (C)	Reactor	Biotite (g)	Flow Rate (mL min^{-1})[a]	Time (h)	% Diss[b]	Meas. pH[c]	Calc. pH[d]	log Rate$_{Me}$ (moles biotite m^{-2} s^{-1})[e]				
								Si	Al	Fe	Mg	K
25	A	2.0083	0.247±0.016	312.00	3.01	12.950	12.950	$-11.60^{+0.05}_{-0.05}$	$-11.36^{+0.05}_{-0.05}$	$-12.07^{+0.05}_{-0.05}$	$-14.00^{+0.12}_{-0.17}$	$-11.22^{+0.05}_{-0.06}$
40			0.252±0.003	144.58	0.43	13.150	12.685	$-11.45^{+0.05}_{-0.05}$	$-11.22^{+0.05}_{-0.05}$	$-11.92^{+0.05}_{-0.05}$	$-14.05^{+0.11}_{-0.14}$	$-11.49^{+0.05}_{-0.06}$
55			0.252±0.003	141.67	0.45	13.030	12.165	$-11.34^{+0.05}_{-0.06}$	$-11.30^{+0.05}_{-0.05}$	$-11.87^{+0.05}_{-0.05}$	$-13.72^{+0.16}_{-0.26}$	$-11.48^{+0.05}_{-0.06}$
70			0.263±0.010	362.25	1.08	13.060	11.851	$-11.44^{+0.07}_{-0.09}$	$-11.51^{+0.05}_{-0.05}$	$-12.05^{+0.05}_{-0.05}$	$-13.71^{+0.09}_{-0.11}$	$-11.55^{+0.05}_{-0.06}$
55			0.281±0.006	142.67	0.13	13.110	12.245	$-11.75^{+0.09}_{-0.12}$	$-11.85^{+0.05}_{-0.06}$	$-12.38^{+0.05}_{-0.05}$	$-13.84^{+0.07}_{-0.09}$	BD[f]
40			0.291±0.004	144.16	0.08	13.250	12.788	$-12.04^{+0.05}_{-0.05}$	$-11.92^{+0.05}_{-0.05}$	$-12.67^{+0.05}_{-0.05}$	$-13.89^{+0.08}_{-0.09}$	BD[f]
25			0.297±0.003	144.34	0.01	13.070	13.070	$-12.75^{+0.16}_{-0.24}$	$-12.04^{+0.05}_{-0.05}$	$-12.87^{+0.15}_{-0.22}$	$-14.22^{+0.13}_{-0.18}$	BD[f]
Totals				1391.67	5.19							
70	B	1.9986	0.254±0.011	359.73	3.51	13.110	11.986	$-11.48^{+0.05}_{-0.06}$	$-11.52^{+0.05}_{-0.05}$	$-11.83^{+0.05}_{-0.05}$	$-13.62^{+0.08}_{-0.10}$	$-11.27^{+0.05}_{-0.06}$
55			0.266±0.005	142.67	0.13	13.080	12.214	$-11.78^{+0.05}_{-0.06}$	$-11.68^{+0.05}_{-0.05}$	$-12.15^{+0.05}_{-0.05}$	$-13.78^{+0.05}_{-0.05}$	BD[f]
40			0.278±0.006	144.16	0.06	13.210	12.747	$-12.30^{+0.06}_{-0.07}$	$-11.78^{+0.05}_{-0.05}$	$-12.41^{+0.05}_{-0.05}$	$-13.83^{+0.07}_{-0.09}$	BD[f]
25			0.291±0.006	144.34	0.03	13.110	13.111	$-12.38^{+0.09}_{-0.12}$	$-11.79^{+0.05}_{-0.05}$	$-12.68^{+0.05}_{-0.05}$	$-13.56^{+0.32}_{BD}$	BD[f]
Totals				790.90	3.73							

[a]Flow rates shown represent average rates for the duration of the experiment excluding scheduled excursions to higher flow rates and the decrease in flow rates during the final 43 h. The error is one standard deviation.
[b]Percent of mass dissolved is based on Si release.
[c]Samples from intervals at 40, 55, and 70°C were allowed to equilibrate to room temperature (approximately 23°C) before pH was measured.
[d]The pH measured at room temperature was used as input to the geochemical modeling program The Geochemist's Workbench® 4.0.3 which was used to calculate the equivalent pH at the experimental temperature.
[e] Uncertainties in the rates were determined by error propagation based on uncertainties in flow rate, BET surface area (5%), ICP-OES analysis (standard deviation of 3 replicate readings or 10%, whichever was greater), and average concentration (standard deviation of the readings comprising the average). Where the lower limit is designated "BD", after error propagation the final rate was negative.
[f]BD: effluent concentration was below the analytical detection limit.

Table 4. Reacted biotite.

Exp ID	Original Surface Area (m^2 g^{-1})	Final Surface Area (m^2 g^{-1})	Ratio Final/Original	Total Hours of Diss.	% Dissolved
1-10	4.6226±0.0050	53.5367±0.2693	11.58	193	58.18
3-50R	4.6226±0.0050	6.4501±0.0491	1.40	1753	38.90
6B-10	5.1090±0.0077	7.3008±0.0715	1.43	2041	1.94
6-10	5.1090±0.0077	6.7675±0.0576	1.32	2064	2.42
12-70	5.1090±0.0077	9.2809±0.0332	1.82	600	6.91

Table 5. Summary of *X* mg release calculations (*X* = 15 and 30).

			15 mg release			30 mg release		
Exp. ID	Inlet pH	Buffer	Time (h)	Effluent pH	log $Rate_{Me,15mg}$ (moles Bt m^{-2} s^{-1})	Time (h)	Effluent pH	log $Rate_{Me,30mg}$ (moles Bt m^{-2} s^{-1})
1-25	1		1.1	1.048	-8.60	2.8	1.048	-8.70
2-25	2		1.4	2.045	-8.69	9.0	2.045	-9.20
3-25	3		8.8	3.810	-9.50	77	3.128	-10.14
4-25	4		77	4.485	-10.44	245	4.240	-10.64
5-25R	5		149	6.009	-10.94	914	5.165	-11.43
8-25	8		148	6.901	-10.94	2311[a]	*b*	-11.83
8B-25R	8	H_3BO_3	219	7.954	-11.11	2229[a]	*b*	-11.82
9B-25R	9	H_3BO_3	75	9.022	-10.65	603	8.995	-11.25
10B-25	10	H_3BO_3	75	10.043	-10.43	556	9.994	-10.99
11-25	11		75	11.009	-10.42	1091[a]	*b*	-11.28
12-25	12		28	11.967	-10.00	1085[a]	*b*	-11.29
13-25	13		3.5	13.204	-9.09	365	12.906	-10.81
14-25	14		2.1	13.930	-8.87	50	13.620	-9.95

[a]Time was extrapolated from the available data since < 30 mg was dissolved during the experiment.
[b]Not applicable since time was extrapolated. In Fig. 2 inlet pH has been substituted.

Table 6. Activation energies.

pH	Ea (kJ mol^{-1})	pH	Ea (kJ mol^{-1})
1	48.3	7	6.0
2	41.3	11	38.6
3	34.2	12	42.4
4	27.3	13	46.2
5	20.1	14	49.9
6	13.1		

Figure Captions

Fig. 1. Release rates at 25°C for (a) Si and Al, and (b) Fe and Mg, as a function of pH with rates from Samson et al., 2005, included for comparison. Error bars that fall within the dimensions of the data symbol have been omitted.

Fig. 2. Si release rates based on mass dissolved at 25°C for X = 15 mg and X = 30 mg (Eqn. 6). Included for comparison are Si steady-state release rates from the current study, rates from Samson et al., 2005, for pHs 7-14, and rates from Malmström and Banwart, 1997, for pHs 2-10, all at 25°C. Circled data points indicate experiments where < 30 mg was dissolved so time, t, was extrapolated from the available data.

Fig. 3. Release rates for all elements as a function of pH at (a) 10°C, (b) 25°C, (c) 50°C, and (d) 70°C. Error bars that extend beyond the dimensions of the data symbol are included for K and Ti (see Fig. 4 for error bars for remaining elements). Where an arrow replaces the lower bar, after error propagation the final rate was negative.

Fig. 4. Release rates for (a) Si, (b) Al, (c) Fe, and (d) Mg as a function of pH and T. Error bars that fall within the dimensions of the data symbol have been omitted. Where an arrow replaces the lower bar, after error propagation the final rate was negative.

Fig. 5. Results of the multi-T experiments at pH 13 for (a) reactor A, and, following the addition of reactor B at ~ 600 h, for (b) Si, (c) Al, and (d) Fe for both reactors. Lines indicating flow rates are referenced to the right axis. Solid vertical lines denote T changes.

Fig. 6. (a) Linear regressions of Si release rates at 10, 25, 50 and 70°C for pHs 1-7 and 10, 25, and 50°C for pHs 11-14 (data points omitted for clarity). (b) Activation energies for biotite dissolution based on Si release for pHs 1-7 and 11-14; trend interpolated for pHs 7-11.

Fig. 7. Saturation indices for phlogopite, the pure-Mg analogue for biotite, and annite, the pure-Fe analogue, calculated with GWB. Biotite saturation indices were estimated by interpolating between the two analogues based on stoichiometric values for Fe and Mg in the biotite.

Fig. 8. XRD pattern for pH 13, multi-T experiment sample A. Biotite peaks labeled with their Miller indices (*hkl*) are indicated by vertical lines.

Fig. 9. XRD patterns for selected samples from the single-T experiments. Biotite peaks labeled with their Miller indices (*hkl*) are indicated by vertical lines.

Fig. 10. XRD pattern for sample 14-50R (pH 14, 50°C). Biotite peaks labeled with their Miller indices (*hkl*) are indicated by solid vertical lines; dotted lines mark the locations of the sample's 001 peak and its multiples (Miller indices shown at the base of the lines).

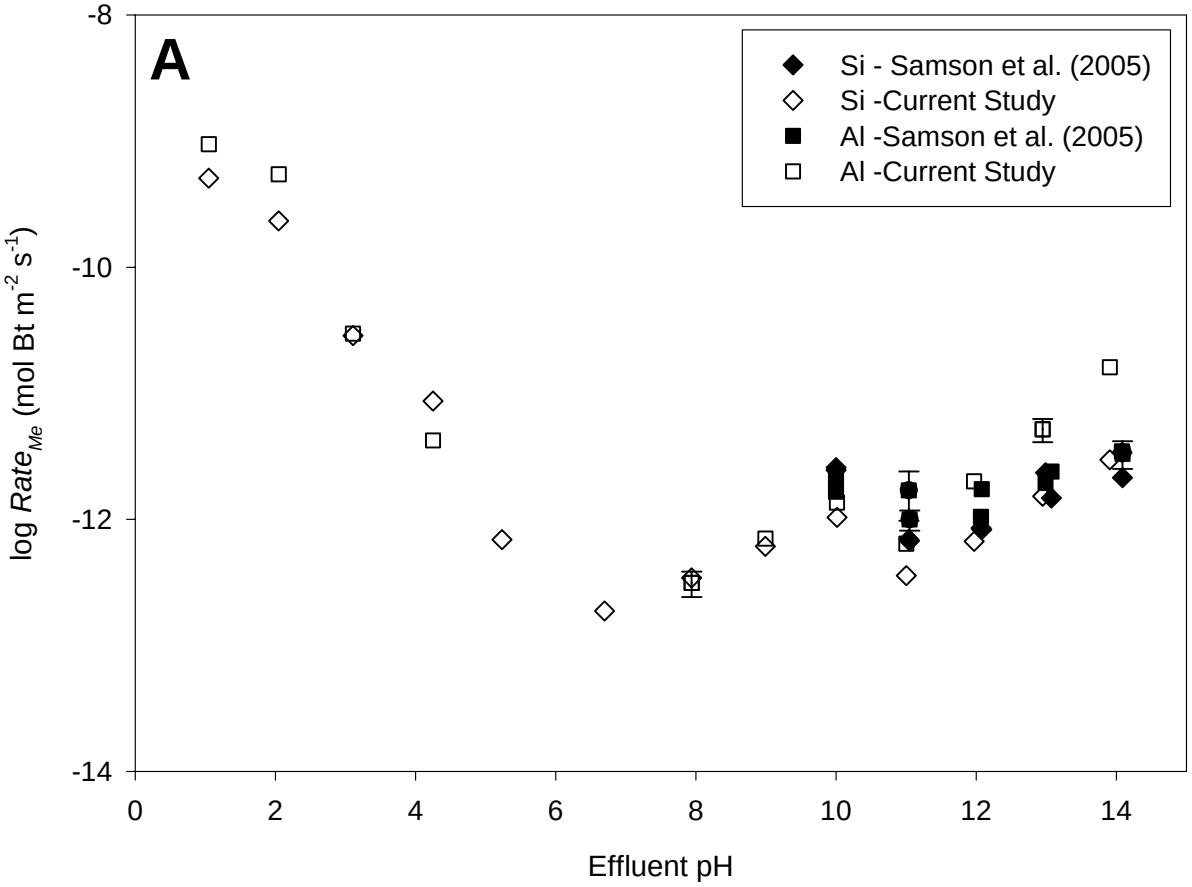
A
Si - Samson et al. (2005)
Si -Current Study
Al -Samson et al. (2005)
Al -Current Study
log Rate_Me (mol Bt m-2 s-1)
-8
-10
-12
-14
0
2
4
6
8
10
12
14
Effluent pH

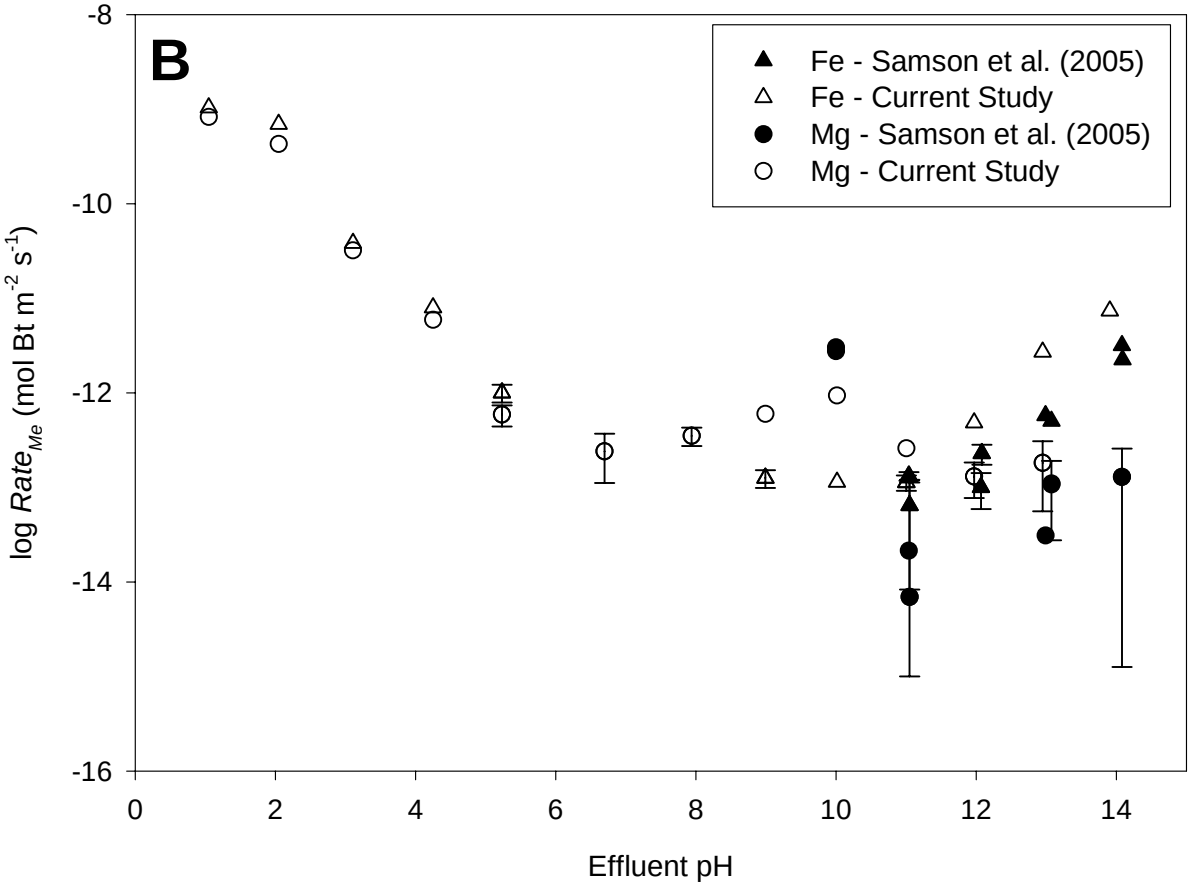
B
Fe - Samson et al. (2005)
Fe - Current Study
Mg - Samson et al. (2005)
Mg - Current Study
log Rate_Me (mol Bt m-2 s-1)
-8
-10
-12
-14
-16
0
2
4
6
8
10
12
14
Effluent pH

Fig. 1

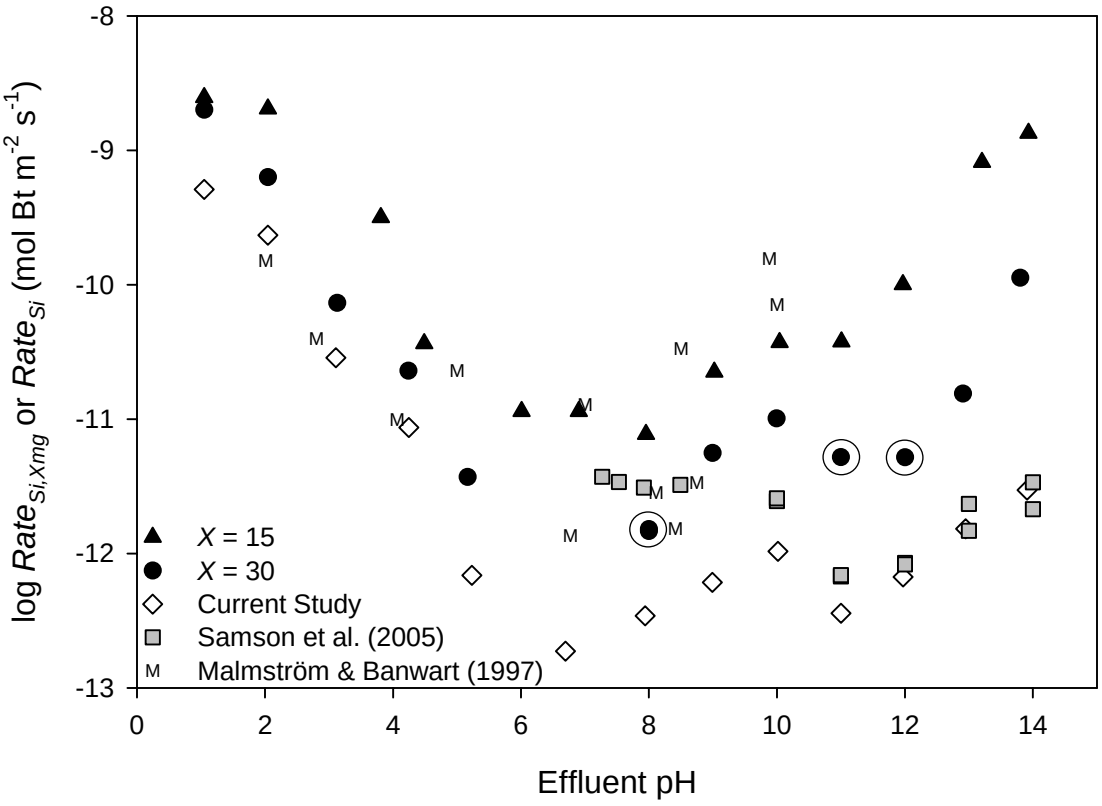
-8
-9
-10
-11
-12
-13
0
2
4
6
8
10
12
14
log $Rate_{Si,Xmg}$ or $Rate_{Si}$ (mol Bt m^{-2} s^{-1})
Effluent pH
X = 15
X = 30
Current Study
Samson et al. (2005)
M
Malmström & Banwart (1997)

Fig. 2

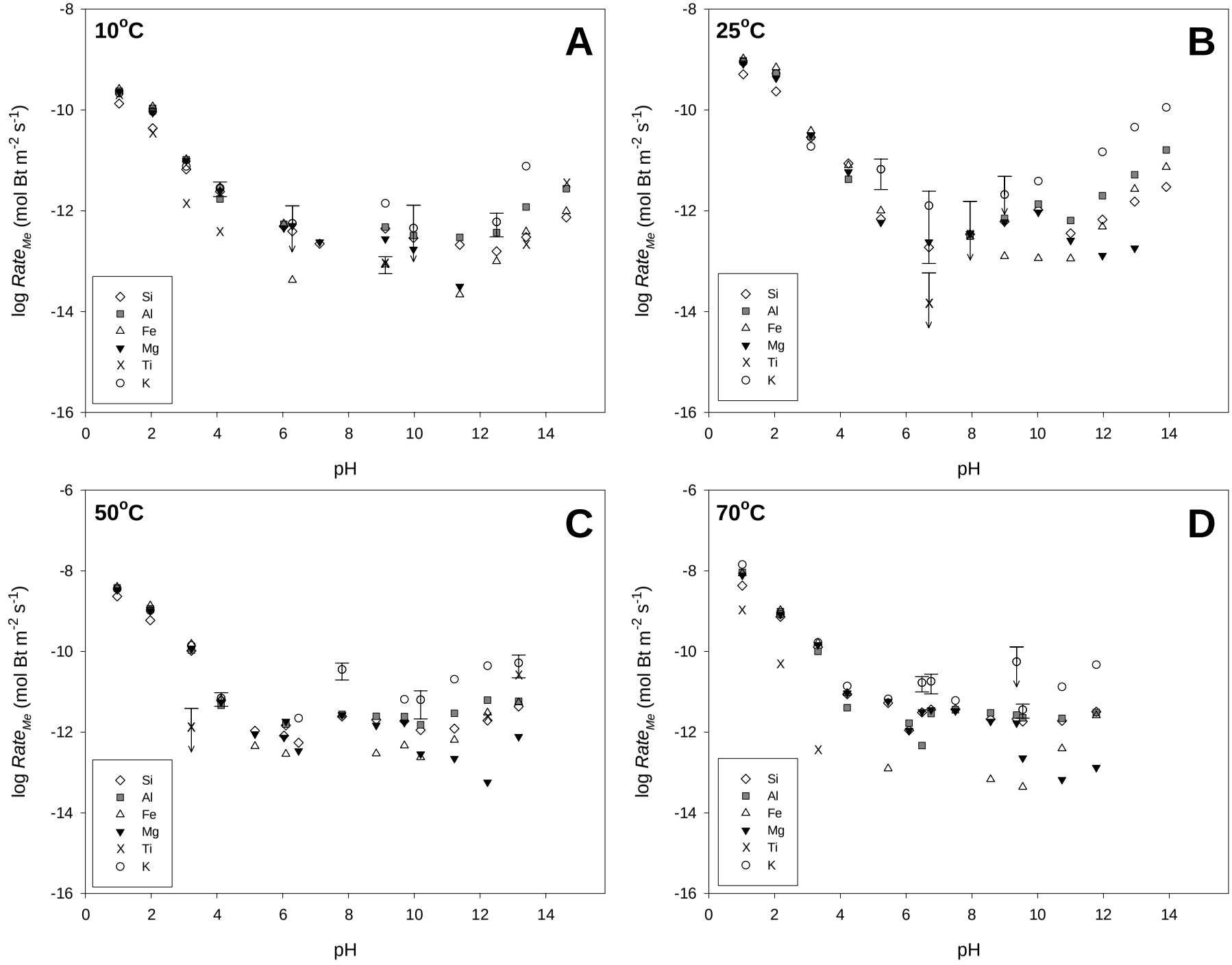

Fig. 3

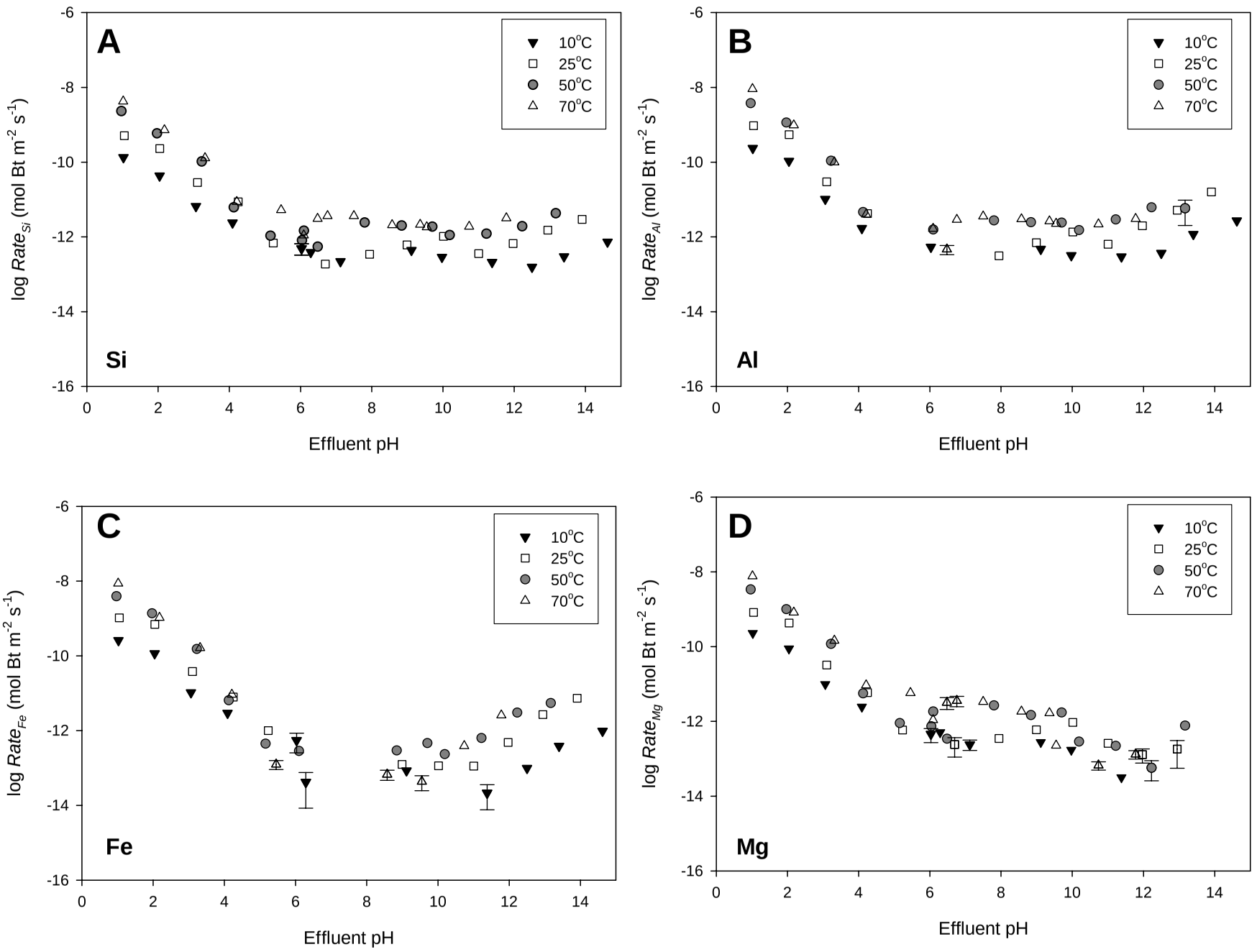
A
Si
B
Al
C
Fe
D
Mg
10°C
25°C
50°C
70°C
log Rate_Si (mol Bt m-2 s-1)
log Rate_Al (mol Bt m-2 s-1)
log Rate_Fe (mol Bt m-2 s-1)
log Rate_Mg (mol Bt m-2 s-1)
Effluent pH
-6
-8
-10
-12
-14
-16
0
2
4
6
8
10
12
14

Fig. 4

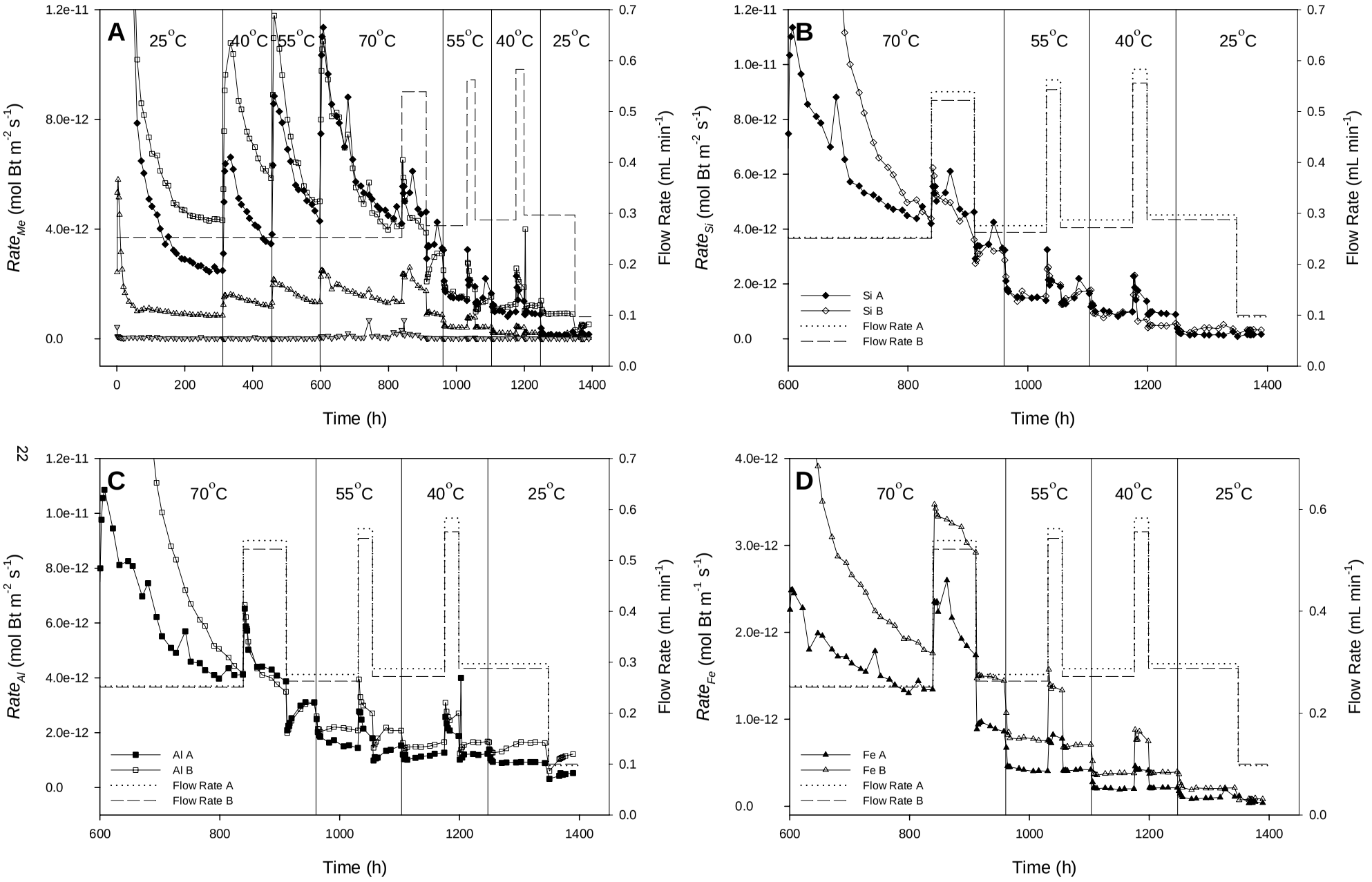
A
25°C
40°C
55°C
70°C
55°C
40°C
25°C
Rate_Me (mol Bt m-2 s-1)
Flow Rate (mL min-1)
Time (h)
B
70°C
55°C
40°C
25°C
Rate_Si (mol Bt m-2 s-1)
Si A
Si B
Flow Rate A
Flow Rate B
Time (h)
C
70°C
55°C
40°C
25°C
Rate_Al (mol Bt m-2 s-1)
Al A
Al B
Flow Rate A
Flow Rate B
Time (h)
D
70°C
55°C
40°C
25°C
Rate_Fe (mol Bt m-1 s-1)
Fe A
Fe B
Flow Rate A
Flow Rate B
Time (h)

Fig. 5

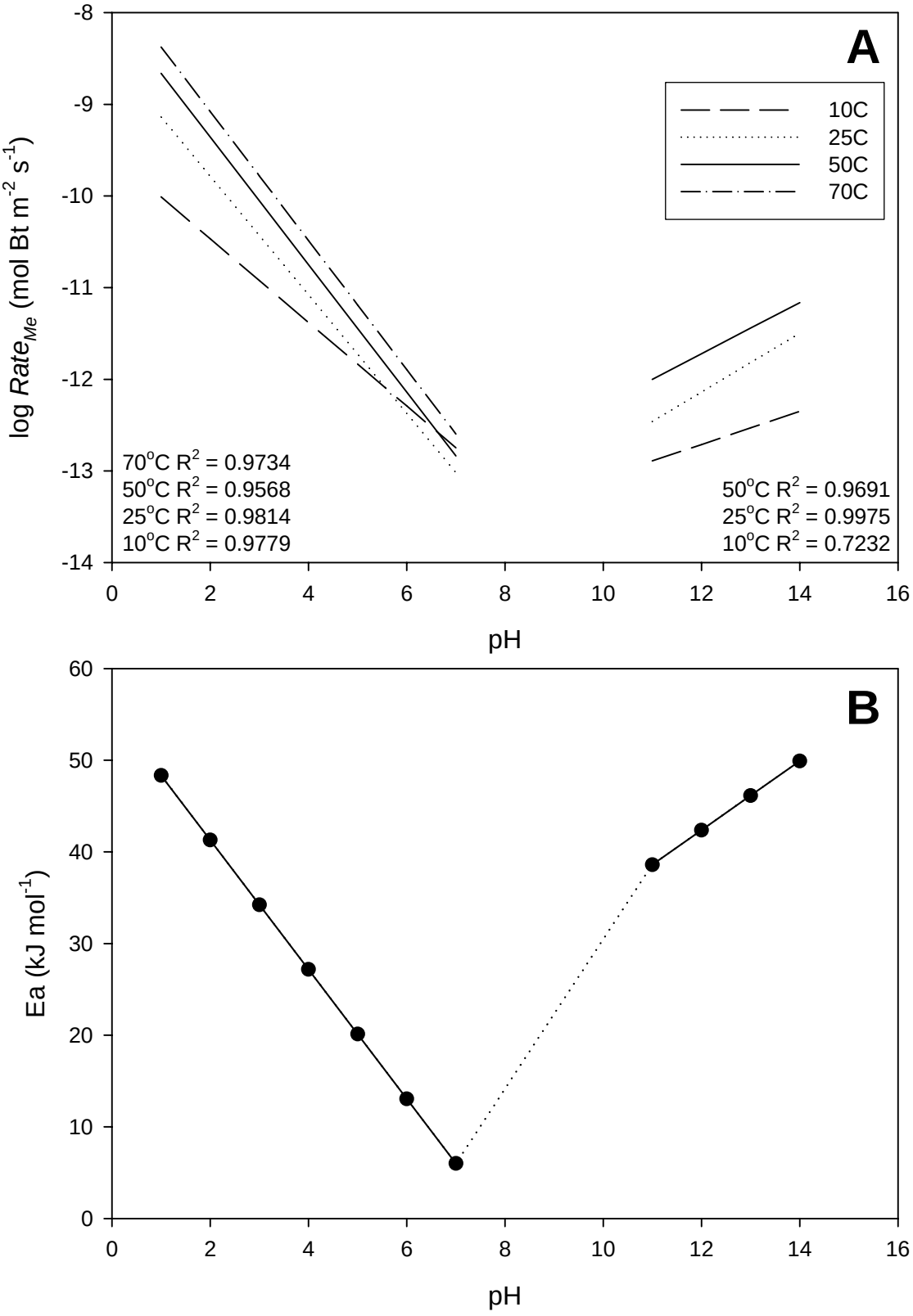
A
10C
25C
50C
70C
log Rate$_{Me}$ (mol Bt m^{-2} s^{-1})
70°C R^2 = 0.9734
50°C R^2 = 0.9568
25°C R^2 = 0.9814
10°C R^2 = 0.9779
50°C R^2 = 0.9691
25°C R^2 = 0.9975
10°C R^2 = 0.7232
pH
B
Ea (kJ mol^{-1})
pH

Figure 6

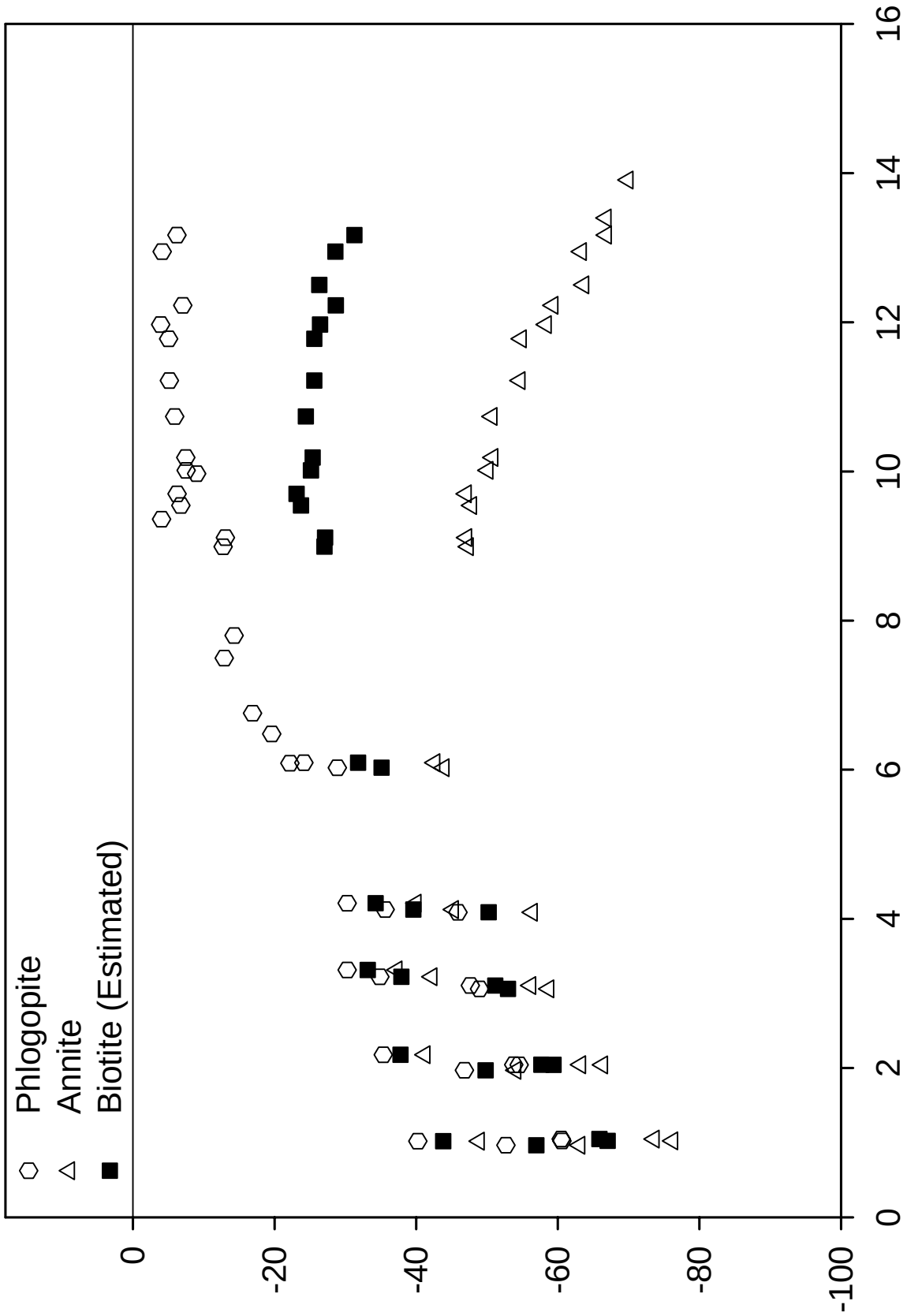
Phlogopite
Annite
Biotite (Estimated)
log Q/K
0
-20
-40
-60
-80
-100
0
2
4
6
8
10
12
14
16
Final pH

Fig. 7

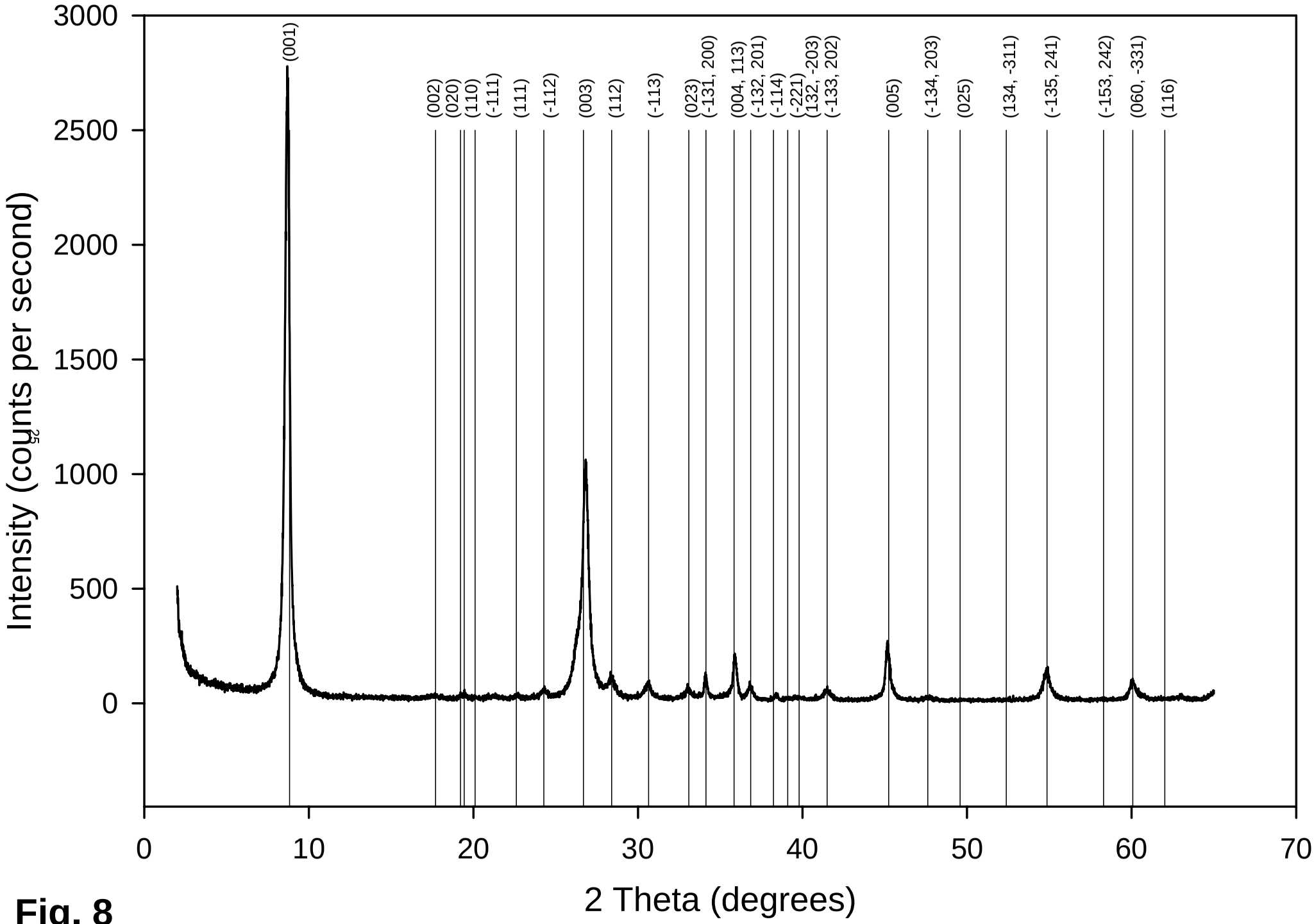
3000
2500
2000
1500
1000
500
0
Intensity (counts per second)
0
10
20
30
40
50
60
70
2 Theta (degrees)
(001)
(002)
(020)
(110)
(-111)
(111)
(-112)
(003)
(112)
(-113)
(023)
(-131, 200)
(004, 113)
(-132, 201)
(-114)
(-221)
(132, -203)
(-133, 202)
(005)
(-134, 203)
(025)
(134, -311)
(-135, 241)
(-153, 242)
(060, -331)
(116)

Fig. 8

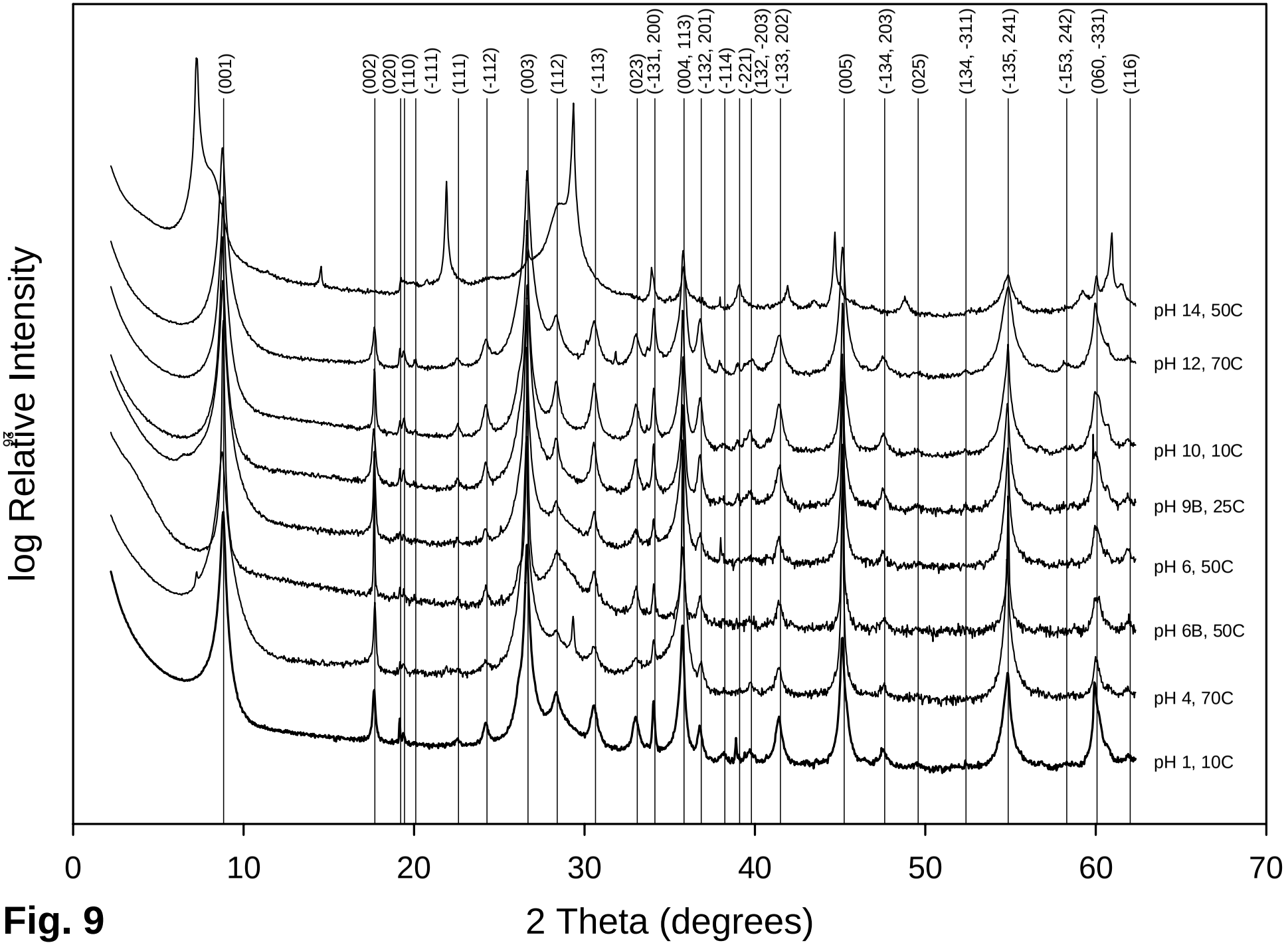
log Relative Intensity
2 Theta (degrees)
0
10
20
30
40
50
60
70
(001)
(002)
(020)
(110)
(-111)
(111)
(-112)
(003)
(112)
(-113)
(023)
(-131, 200)
(004, 113)
(-132, 201)
(-114)
(-221)
(132, -203)
(-133, 202)
(005)
(-134, 203)
(025)
(134, -311)
(-135, 241)
(-153, 242)
(060, -331)
(116)
pH 14, 50C
pH 12, 70C
pH 10, 10C
pH 9B, 25C
pH 6, 50C
pH 6B, 50C
pH 4, 70C
pH 1, 10C

Fig. 9

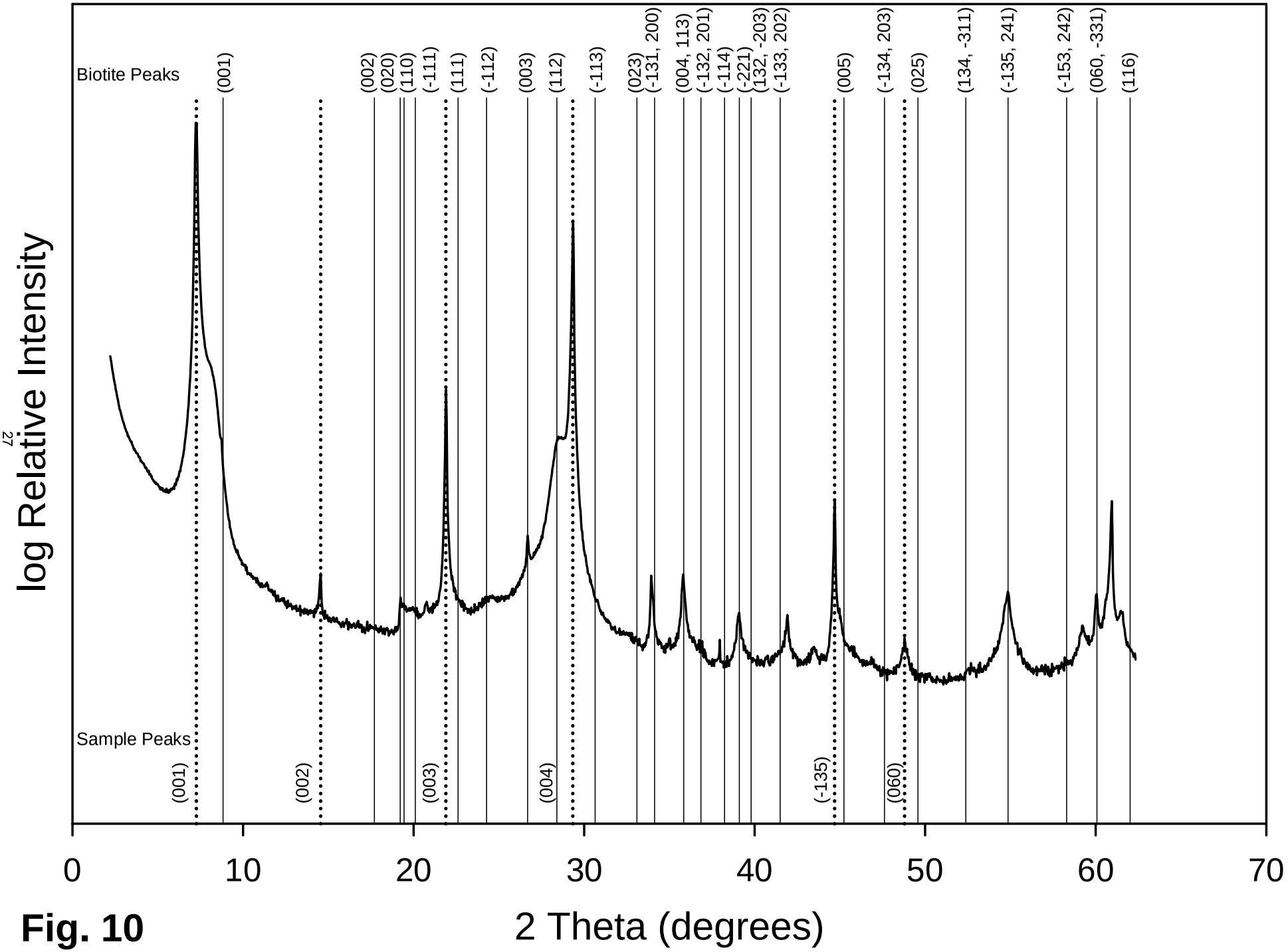
log Relative Intensity
2 Theta (degrees)
0
10
20
30
40
50
60
70
Biotite Peaks
(001)
(002)
(020)
(110)
(-111)
(111)
(-112)
(003)
(112)
(-113)
(023)
(-131, 200)
(004, 113)
(-132, 201)
(-114)
(-221)
(132, -203)
(-133, 202)
(005)
(-134, 203)
(025)
(134, -311)
(-135, 241)
(-153, 242)
(060, -331)
(116)
Sample Peaks
(001)
(002)
(003)
(004)
(-135)
(060)

Fig. 10

References

Banfield J. F. and Eggleton R. A. (1988) Transmission electron microscope study of biotite weathering. *Clays and Clay Minerals* 36(1), 47-60.

Bethke C. M. (2002) The Geochemist's Workbench® 4.0. University of Illinois.

Busey R. H. and Mesmer R. E. (1977) Ionization equilibria of silicic acid and polysilicate formation in aqueous sodium chloride solutions to 300°C. *Inorganic Chemistry* 16, 2444-2450.

Ferrow E. A., Kalinowski B. E., Veblen D. R., and Schweda P. (1999) Alteration products of experimentally weathered biotite studied by high-resolution TEM and Mössbauer spectroscopy. *European Journal of Mineralogy* 11(6), 999-1010.

ICDD. (2001) *Mineral Powder Diffraction File Mineral Search Manual*. International Centre for Diffraction Data.

ICDD. (2005) Powder Diffraction File. International Centre for Diffraction Data.

Jeong G. Y. and Kim H. B. (2003) Mineralogy, chemistry, and formation of oxidized biotite in the weathering profile of granitic rocks. *American Mineralogist* 88, 352-364.

Kogure T. and Murakami T. (1996) Direct identification of biotite/vermiculite layers in hydrobiotite using high-resolution TEM. *Mineralogical Journal* 18(4), 131-137.

Malmström M. E. and Banwart S. A. (1997) Biotite dissolution at 25°C: The pH dependence of dissolution rate and stoichiometry. *Geochimica et Cosmochimica Acta* 61(14), 2779-2799.

Materials Data I. (2005) JADE.

Samson S. D., Nagy K. L., and Worth C. B., III. (2005) Transient and quasi-steady-state dissolution of biotite at 22-25°C in high pH, sodium, nitrate, and aluminate solutions. *Geochimica et Cosmochimica Acta* 69(2), 399-413.

Samson S. D., Stillings L. L., and Eggleston C. M. (2000) The depletion and regeneration of dissolution-active sites at the mineral-water interface: I. Fe, Al, and In sesquioxides. *Geochimica et Cosmochimica Acta* 64(20), 3471-3484.

Stoessell R. K. (1988) 25°C and 1 atm dissolution experiments of sepiolite and kerolite. *Geochimica et Cosmochimica Acta* 52, 365-374.

Wesolowski D. J. and Palmer D. A. (1994) Aluminum speciation and equilibria in aqueous solution. V. Gibbsite solubility at 50°C and pH 3-9 in 0.1 molal NaCl solutions (a general model for aluminum speciation; analytical methods). *Geochimica et Cosmochimica Acta* 58(14), 2947-2969.

Task 2. Dissolution of Quartz as a Function of pH, Temperature, and Aluminate Concentration

Two papers were published based on previous EMSP research conducted by Post-Doctoral Associate Barry Bickmore (now Associate Professor at Brigham Young University). The first of these papers shows that aluminate inhibits the dissolution rate of quartz in basic pH solutions based on new experimental data. The second paper applies a graphical analysis technique to a published compilation of quartz dissolution rates to show that there is an additional mechanism for quartz dissolution at basic pH which is they hydrolysis of Si centers in the quartz structure by hydroxyl ions.

Bickmore B. R., Nagy K. L., Gray, A. K., and A. R. Brinkerhoff, 2006, The effect of $Al(OH)_4^-$ on the dissolution rate of quartz, *Geochimica et Cosmochimica Acta* 70, 290-305.

Bickmore B. R., Wheeler J. C., Bates B., Nagy K. L., Eggett D. L., 2008, Reaction pathways for quartz dissolution determined by statistical and graphical analysis of macroscopic experimental data. *Geochimica et Cosmochimica Acta* 72, 4521-4536.

Abstract from Bickmore et al., 2006:

The influence of $Al(OH)_4$ on the dissolution rate of quartz at pH 10–13 and 59–89 °C was determined using batch experiments. $Al(OH)_4$ at concentrations below gibbsite solubility depressed the dissolution rate by as much as 85%, and this effect was greater at lower pH and higher $Al(OH)_4$ concentration. Dissolution rates increased with increasing temperature; however, the percent decrease in rate due to the presence of $Al(OH)_4$ was invariant with temperature for a given H^+ activity and $Al(OH)_4$ concentration. These data, along with what is known about Al–Si interactions at high pH, are consistent with $Al(OH)_4$ and Na^+ co-adsorbing on silanol sites and passivating the surrounding quartz surface. The observed pH dependence, and lack of temperature dependence, of inferred $Al(OH)_4$ sorption also supports the assumption that the acid–base behavior of the surface silanol groups has only a small temperature dependence in this range. A Langmuir-type adsorption model was used to express the degree of rate depression for a given in situ pH and $Al(OH)_4$ concentration. Incorporation of the rate data in the absence of aluminate into models that assume a first-order dependence of the rate on the fraction of deprotonated silanol sites was unsuccessful. However, the data are consistent with the hypothesis proposed in the literature that two dissolution mechanisms may be operative in alkaline solutions: nucleophilic attack of water on siloxane bonds catalyzed by the presence of a deprotonated silanol group and OH^- attack catalyzed by the presence of a neutral silanol group. The data support the dominance of the second mechanism at higher pH and temperature.

Abstract from Bickmore et al., 2008:

In light of recent work on the reactivity of specific sites on large (hydr)oxo-molecules and the evolution of surface topography during dissolution, we examined the ability to extract molecular-scale reaction pathways from macroscopic dissolution and surface charge measurements of powdered minerals using an approach that involved regression of multiple datasets and statistical graphical analysis of model fits. The test case (far-from-equilibrium quartz dissolution from 25 to 300 °C, pH 1 to 12, in solutions with $[Na^+] \leq 0.5$ M) avoids the objections to this goal raised in these recent studies. The strategy was used to assess several mechanistic rate laws, and was more powerful in

distinguishing between models than the statistical approaches employed previously. The best-fit model included three mechanisms—two involving hydrolysis of Si centers by H_2O next to neutral (>Si-OH^0) and deprotonated (>Si-O^-) silanol groups, and one involving hydrolysis of Si centers by OH^-. The model rate law is

$$\frac{dSi}{dt}\left(mol/m^2 s\right) = e^{-8.9\pm0.8} Te^{\left(\frac{-67.5\pm2.7\,kJ/mol}{RT}\right)}\left(\theta_{>SiOH}\right) + e^{3.6\pm0.7} Te^{\left(\frac{-82.8\pm2.1\,kJ/mol}{RT}\right)}\left(\theta_{>SiO^-}\right) + e^{6.7\pm1.8} Te^{\left(\frac{-77.5\pm6.0\,kJ/mol}{RT}\right)} a_{OH^-} \quad (\pm 0.7 \text{ log units}),$$

where $\theta_{>SiOH}$ and $\theta_{>SiO^-}$ are the fraction of surface silanol groups in the neutral and deprotonated forms, and a_{OH^-} is the bulk activity of OH^-. The fitted $\Delta H^{\ddagger}$ value (67.5 kJ/mol) for the dominant low-pH mechanism indicates that the model lacks a fourth mechanism involving protonation of bridging oxygens on siloxane (>Si-O-Si<) groups, which cannot be included because the acidity of bridging oxygens is unknown. Further progress on this and other, more complex systems requires development of more predictive and realistic models of surface speciation.

Task 3. Dissolution of Plagioclase Feldspar in Simulated Tank Solutions

This task resulted in the completion of one Master's Thesis at the University of Illinois at Chicago, a brief summary of which is given below.

William Bates, 2005, Dissolution of labradorite at 25 °C in high pH, sodium-nitrate, and simplified Hanford tank waste solutions, Master of Science Thesis, University of Illinois at Chicago, 97 pp.

Dissolution rates (Tables 7 and 8, Figure 11) of labradorite feldspar in basic (pH 8 to 12), high sodium nitrate, and simplified tank waste solutions were measured using stirred-flow reactors at 25°C to simulate likely conditions at the Hanford Site. Steady-state labradorite dissolution rates based on Si release were slowest at pH 8 ($10^{-11.73}$ mol labradorite m^{-2} s^{-1}) and increased as the solution became more basic (pH 12; $10^{-10.70}$ mol labradorite m^{-2} s^{-1})). Labradorite dissolution rates in sodium nitrate and tank waste solutions were 55 and 28 % slower than that obtained in a simple pH 10 solution. Thermodynamic calculations indicate that sodium boltwoodite would precipitate in < 2 hours in reactions between a simulated labradorite microfracture environment (surface area to volume ration of 520 m^2 L^{-1}) and sodium nitrate or simulated BX-102 tank waste solutions. Initial transient releases of Ca in the sodium nitrate and tank waste solutions, conducted only at pH 10, were greater than the Ca transient in a simple pH 10 solution by 240 and 67 % respectively. Transient releases of Si and Al were also 42 and 37 % greater in the tank waste solution than in the simple pH 10 solution. Precipitation of secondary phases such as monohydrocalcite in the simulated BX-102 tank waste, faujasite in the simple pH 9 and simulated tank waste solutions, and gibbsite in all solutions at or below pH 10 were indicated based on dissolution rates, X-ray diffraction data and/or saturation state calculations (Figure 12).

Table 7. Initial mass, calculated final mass, calculated final surface area and flow rate for each experiment.

Experiment Number	Initial pH	Initial Mass (g)	Final Mass[a] (g)	Final Surface Area[b] (m^2/g)	Flow Rate (mL/min)
8	8.00 ± 0.05	1.00050	0.98533	4.1593	0.260 ± 0.004
9	9.00 ± 0.05	1.00202	0.97515	4.0868	0.250 ± 0.004
10	10.00 ± 0.02	1.00030	0.91911	4.0158	0.250 ± 0.004
11	10.00 ± 0.02	0.99940	0.95706	4.0868	0.254 ± 0.017
12	11.00 ± 0.02	1.00654	0.88264	3.9808	0.249 ± 0.010
13	12.00 ± 0.02	1.00882	0.85772	3.9120	0.245 ± 0.009
14	10.00 ± 0.02	1.00274	0.91451	4.0158	0.242 ± 0.011
15	9.00 ± 0.05	1.00171	0.98768	4.0159	0.241 ± 0.008
16	10.00 ± 0.02	1.00175	0.93261	4.0158	0.253 ± 0.002
17	12.00 ± 0.02	1.00004	0.85166	3.9120	0.250 ± 0.007

a. Mass at end of the experiments was calculated from cumulative Si release.

b. Surface Areas of the reacted labradorite were calculated from the dissolution rates based on Si release.

Table 8. Steady-state effluent solution composition and log dissolution rate.j

Experiment Number	pH	Si	Al	Ca	Log Dissolution Rate[b] (moles of labradorite m^{-2} s^{-1})		
8	7.98	1.01	0.03	0.64	$-11.73^{+0.02}_{-0.02}$	$-12.88^{+0.12}_{-0.16}$	$-11.34^{+0.02}_{-0.02}$
9	8.98	1.91	1.07	0.77	$-11.48^{+0.02}_{-0.02}$	$-11.56^{+0.02}_{-0.02}$	$-11.27^{+0.02}_{-0.02}$
10	10.01	5.25	3.56	1.59	$-10.99^{+0.02}_{-0.02}$	$-10.99^{+0.01}_{-0.01}$	$-10.91^{+0.01}_{-0.01}$
11[a]	9.90	4.23	2.45	3.97	$-11.14^{+0.04}_{-0.04}$	$-11.20^{+0.04}_{-0.27}$	$-10.57^{+0.05}_{-0.03}$
12	11.03	8.96	5.40	2.11	$-10.81^{+0.03}_{-0.03}$	$-10.86^{+0.03}_{-0.03}$	$-10.84^{+0.03}_{-0.04}$
13	12.02	11.9	6.97	3.20	$-10.70^{+0.04}_{-0.05}$	$-10.75^{+0.04}_{-0.04}$	$-10.67^{+0.04}_{-0.05}$
14[a]	9.99	7.18	4.53	n.d.	$-10.92^{+0.03}_{-0.03}$	$-10.94^{+0.02}_{-0.03}$	n.d.
15	8.89	0.79	0.21	0.19	$-11.88^{+0.04}_{-0.04}$	$-12.06^{+0.05}_{-0.06}$	$-11.91^{+0.03}_{-0.04}$
16	9.98	9.21	6.45	2.01	$-10.79^{+0.03}_{-0.01}$	$-10.77^{+0.03}_{-0.01}$	$-10.85^{+0.02}_{-0.03}$
17	12.03	15.0	9.17	4.08	$-10.59^{+0.04}_{-0.05}$	$-10.63^{+0.03}_{-0.04}$	$-10.55^{+0.04}_{-0.04}$

[a]. Concentrations and dissolution rates are not steady-state values. Values were calculated at 700 h.
[b]. Dissolution rates were calculated from adjusted surface areas.
n.d. not determined

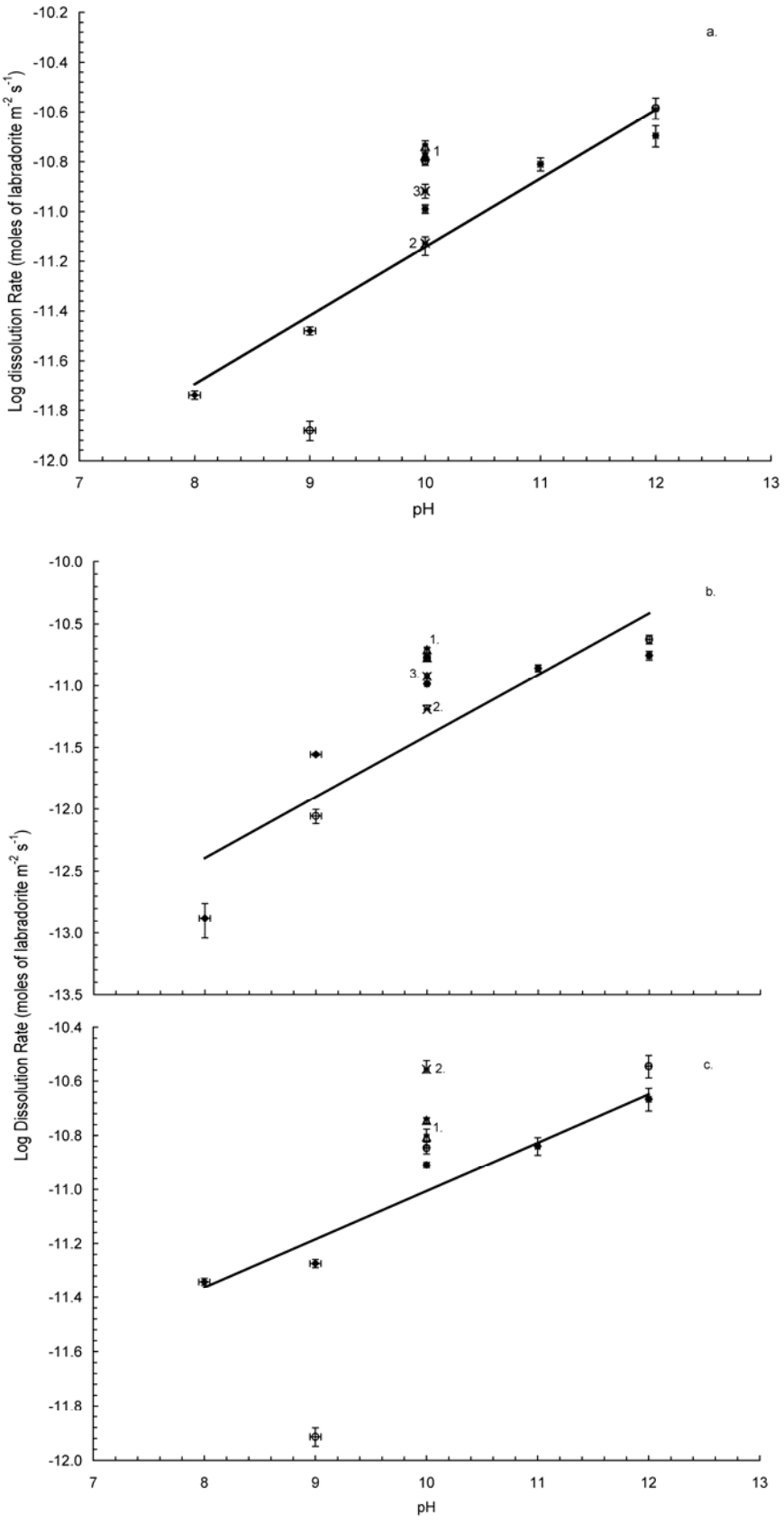

Figure 11. Steady-state dissolution rate of labradorite as a function of pH. a) Log rate as calculated from released Si concentration; b) Log rate as calculated from released Al concentration; c) Log rate as calculated from released Ca concentration; Point labeled 1) quasi-steady-state rate for simple pH 10 solution at 700 h; Point labeled 2) quasi-steady-state rate for pH 10, 2.91 M $NaNO_3$ solution at 700 h; Point labeled 3) quasi-steady-state rate for pH 10, simulated tank waste solution at 700 h

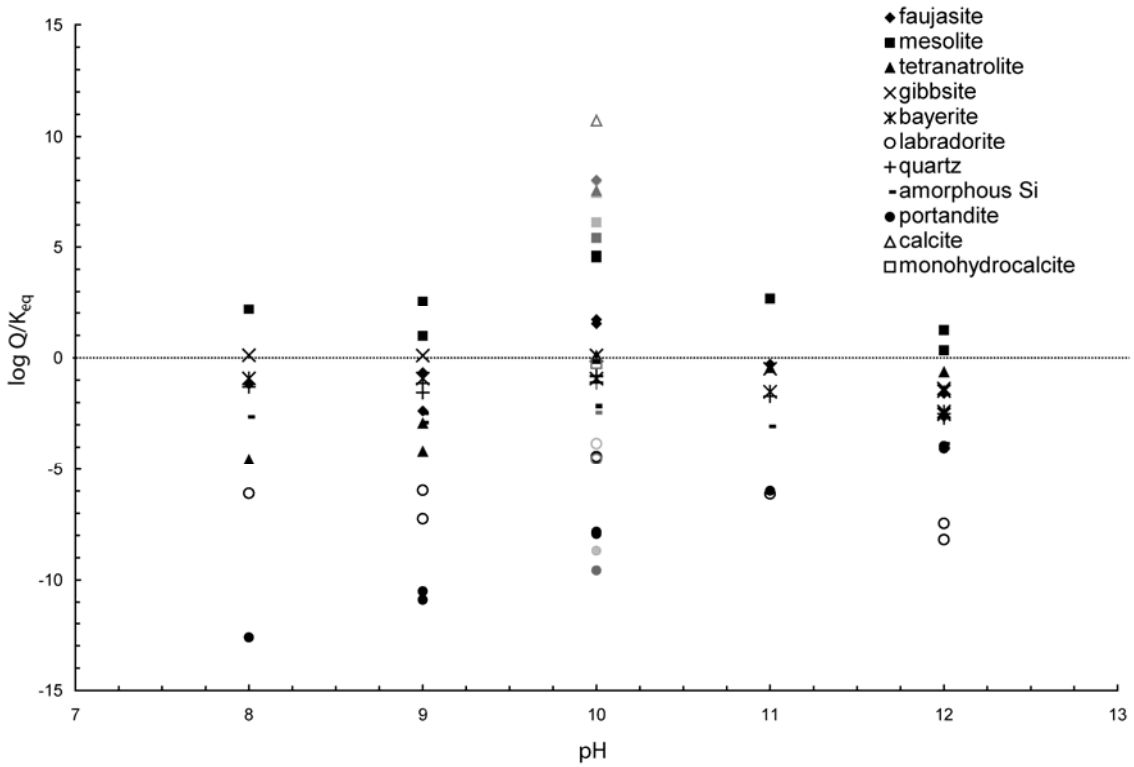

Figure 12. Saturation states of potential secondary phases and labradorite in experimental solutions. The line indicates a saturated solution. The dark gray symbols are for the simulated tank waste experiment at pH 10 and the light gray symbols are for the sodium nitrate experiment at pH 10.

Task 4. Incorporation of Perrhenate in Iron-Oxide Minerals as a Function of pH at 87 °C

One Master's thesis was completed and one manuscript is in preparation.

Rebekah Fitchett, 2006, Rhenium incorporation in aged iron-oxides as a function of pH and chromate concentration, Master of Science Thesis, University of Illinois at Chicago, 78 pp.

Nagy K. L., Fitchett R., and Andjelic D., The uptake of perrhenate in Fe-oxides as a function of pH, concentration, and the presence of other anions at 87 °C, in preparation.

The effects of pH (3, 4, 5, 8, 9, 10), concentration (2.7×10^{-4} to 1×10^{-2} mol Re/L at pH 3, 8, and 10), and other anions (nitrate at 1.5 mol/L, and chromate, bicarbonate, phosphate and sulfate each at 2.7×10^{-4} mol/L at pH 8) on the uptake of perrhenate, a chemical analogue for pertechnetate, in iron oxides were investigated experimentally. Solids were synthesized according to standard techniques at room temperature and immediately aged at 87 °C for approximately 70 hours. The majority of the solid phases under all conditions was hematite, but goethite was present in samples at pH values of 4,

5, and 10 in amounts of 2 to 28%, and at pH 8 with added nitrate and sulfate in amounts of 5 to 9 %.

The amount of Re incorporated in the solids decreased with increasing initial pH of the solutions, and was approximately 200 times higher in solids synthesized at pH 3 than at pH 10 at both 50 and 5000 ppm initial Re solution concentrations (Figure 13). The amount of Re in the

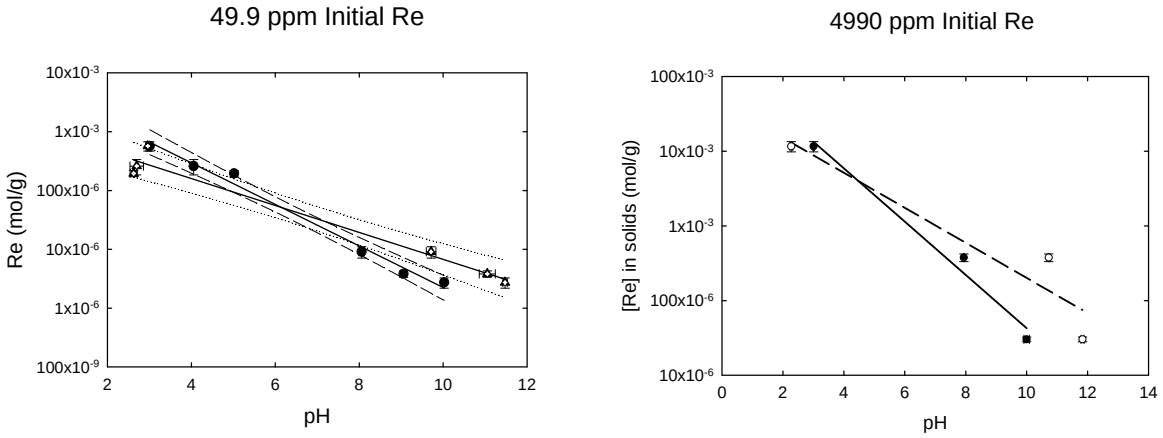

Figure 13. The amount of Re incorporated in Fe-oxides (dominated by hematite) formed from initial solutions containing 50 and 5000 ppm Re decreased by approximately a factor of 200 with increasing pH (solid symbols – initial pH; open symbols - final pH) reflecting in part a decrease in positive surface charge at higher pH and also an increase in the diffracting domain size using powder XRD.

solids as a function of concentration suggested that uptake was controlled by Langmuir adsorption isotherms (Figure 14). Within error, there was no effect of competing anions

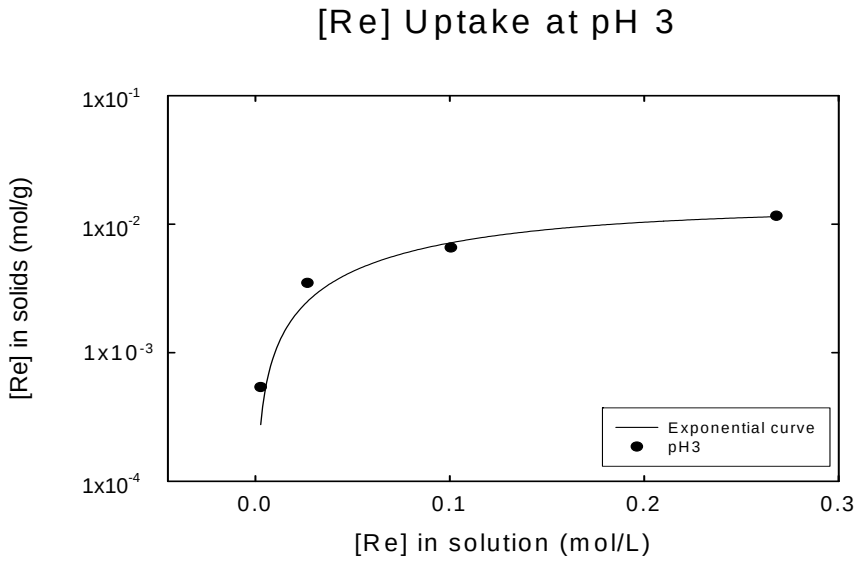

Figure 14. Re uptake in Fe-oxides as a function of initial Re concentration in solution at pH 3. The curve is an exponential fit to the data suggestive of a Langmuir isotherm.

on the uptake of Re at pH 8 with the exception that phosphate may have inhibited the uptake slightly (Figure 15) despite the fact that nitrate, chromate and phosphate were

each taken up to a significant extent by the Fe-oxides. The amount of Re uptake at constant initial Re concentration in solution was inversely correlated to the amount of Cr uptake from variable concentration chromate solutions indicating that chromate successfully competes for surface adsorption sites with Re during the initial synthesis stage (Figure 15).

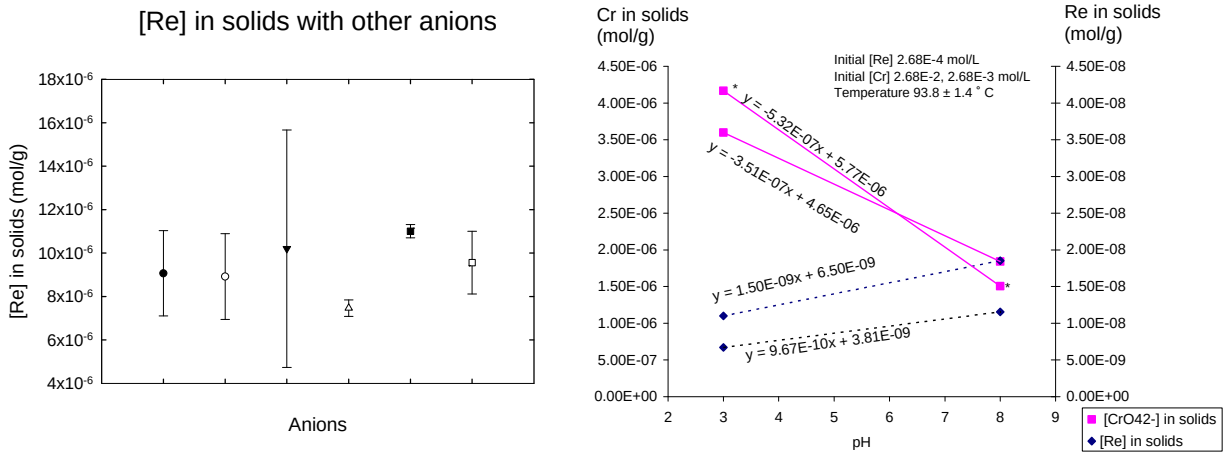

Figure 15. (Left) The amount of Re incorporated in precipitated Fe-oxides from initial pH 8 solutions containing 50 ppm Re (solid diamond) is not changed within error by the addition of 2 m nitrate (square with cross) or 2.1 x 10^{-4} m sulfate (solid upside-down triangle), phosphate (open triangle), bicarbonate (solid square), or chromate (open square). (Right) At higher concentrations of initial chromate, and at slightly higher aging temperature (93 °C) the amount of Re incorporated in the solids is slightly lower and decreases with decreasing pH in contrast to the pattern of Cr incorporation into the solids.

EXAFS and XANES analysis was performed at PNC-CAT at the Advanced Photon Source on the solids with the highest amount of Re. The results indicate that the uptake was in the form of perrhenate bound to surface oxygens of the initially synthesized ferrihydrite grains. Estimates of average grain size using the maximum coverage from the interpreted adsorption isotherms and assuming that adsorption of perrhenate occurs at all the available sites on the Fe-oxide surface showed an increase from low to high pH, consistent with the observed narrowing and sharpening of peaks in powder X-ray diffraction patterns of the solids with increasing pH. However, the estimates suggest grain sizes that are too large when compared with literature data indicating that either adsorption occurs only at selected sites, and/or changes the coarsening behavior of the ferrihydrite particles that are initially precipitated during the synthesis. Additional high resolution transmission electron microscopy results with EELS analysis will be conducted at UIC to attempt to answer this question prior to submission for publication.

Task 5: Formation of Uranium(VI)-Silicate Phases under Ambient Conditions

This work was initiated by Post-Doctoral Associate Ashaki Rouff (now Assistant Professor at Queens College, NYC).

5.1. The Uranyl-Silicato Complex

In groundwater systems, silica derived from dissolution and weathering of silicate rocks can complex with, and ultimately dictate the fate of natural and contaminant uranium. Complexation of orthosilicic acid with oxidized uranium is reported to proceed via the following reaction:

$$UO_2^{2+} + Si(OH)_4 \leftrightarrow UO_2H_3SiO_4^{+} + H^{+} \quad (1\text{-}5)$$

Though much research has been undertaken to quantify the stability of the uranyl-silicato complex, there is considerable variation in obtained constants (Table 9). Though disparity in pH and ionic strength is worth consideration, the inconsistency in equilibrium constant (log K_1) may be attributed to the range of uranium (10^{-5} to 10^{-3} M), and primarily, silicon concentrations implemented. Reported silicon concentration ranges from 10^{-3} to 10^{-2} M—an order of magnitude difference. As polymerization of silicon at 25°C can occur rapidly at concentrations ≥ 2×10^{-3} M (*6*), equilibrium constants determined at higher silicon concentrations may be representative of uranyl complexation with both monomeric and polymeric species (*5*). In light of this, any modeling presented in the current study uses the equilibrium constant reported by Jensen and Choppin (*3*), (log K_1 = -2.92) as their silicate concentrations are sufficiently low to be representative of complexation with monomeric silica (though polymeric species may also be of significance in solutions from studies described in Sections 5.3, 5.4 and 5.6), and as it is the lowest observed constant, it represents a lower limit for concentrations of the uranyl-silicato complex in modeled solutions.

Citation	Ionic Strength M	Si M	U M	pH	Equilibrium constant
Porter and Weber (*1*)	0.2	0.024-0.035	6.40E-04	3.5	-1.95 to -2.03
Satoh and Choppin (*2*)	0.2	0.067		3-4.5	-2.44 ± 0.06
Jensen and Choppin (*3*)	0.1	0.0017	1.00E-05	2.5-5.1	-2.92 ± 0.06
Moll et al. (*4*)	0.3	0.0054	2.30E-05	3.9	-1.67 ± 0.2
Hrnecek and Irlweck (*5*)	0.2	0.01-0.067	2.50E-03	3.3-4.5	-2.21 ± 0.02

Table 9. Equilibrium constants for uranyl-silicato complexes at 25°C in perchlorate solutions as reported in the literature.

Figure 16 shows aqueous speciation with pH for a carbonate-free, 10^{-5} M uranium solution with a silicon concentration close to the solubility of amorphous silica (~120 ppm = 4.3×10^{-3} M (*6*)), and representative of that of groundwater in contact with weathered silicate rocks (~10^{-3} M, Moll et al. (*4*)). The $UO_2H_3SiO_4^{+}{}_{(aq)}$ species is most prevalent at pH ~5-6 and is at least an order of magnitude greater in concentration than

any polymeric uranyl species (Table 10). Significant occurrence of the uranyl-silicato complex within this pH range, at silicon concentrations of ~10^{-3} M, is consistent with the predictions of Jensen and Choppin (*3*), and Moll et al (*4*), at pH = 6 and pH = 5.3, respectively. It should be noted, that speciation models in these studies are based on uranyl-silicate solutions in equilibrium with atmospheric $CO_{2(g)}$. However differences between these and the speciation model presented in Figure 16 appear to be minimal at pH <6. Other species of significance within the pH 5-6 range are $UO_2^{2+}{}_{(aq)}$ and $UO_2OH^{+}{}_{(aq)}$ (Table 10).

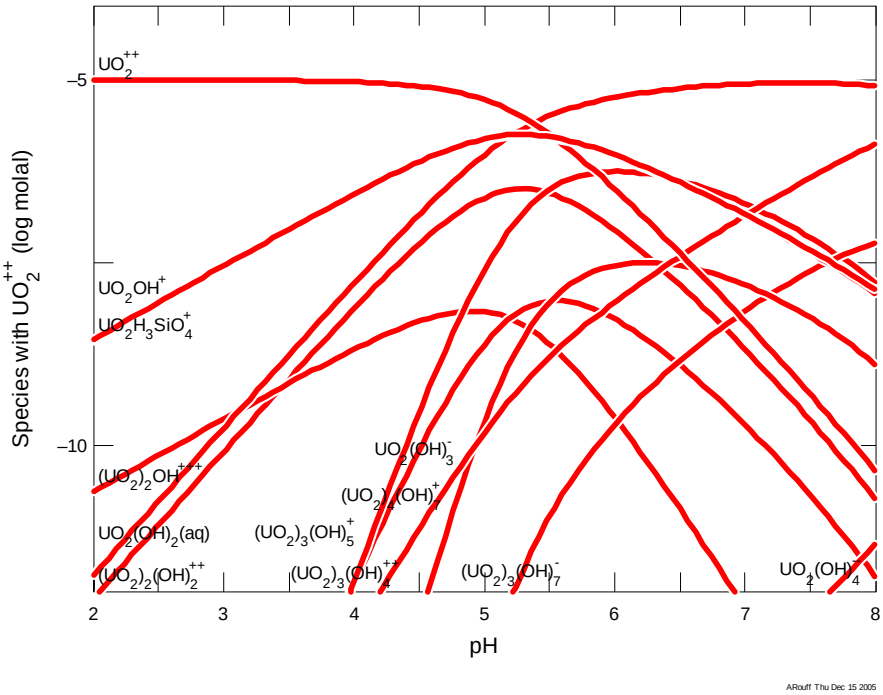

Figure 16. Concentration of U(VI) aqueous species as a function of pH for a 10^{-5} M U, 5×10^{-3} M Si, 0.1 M $NaClO_4$, carbonate-free solution. Concentrations of $UO_2OH^{+}{}_{(aq)}$ and $UO_2H_3SiO_4^{+}{}_{(aq)}$ overlap over the presented pH range. The $UO_2H_3SiO_4^{+}{}_{(aq)}$ complex was assigned an equilibrium constant as determined by Jensen and Choppin (*3*) (Table 9).

Aqueous Species	Concentration M	% Total U
UO_2^{++}	5.37E-06	53.69
UO_2OH^+	1.57E-06	15.71
$UO_2H_3SiO_4^+$	1.52E-06	15.21
$UO_2(OH)_{2(aq)}$	9.52E-07	9.52
$(UO_2)_2(OH)_2^{++}$	2.45E-07	2.45
$(UO_2)_3(OH)_5^+$	2.53E-08	0.25
$(UO_2)_2OH^{+++}$	6.81E-09	0.07
$(UO_2)_3(OH)_4^{++}$	2.44E-09	0.02

Table 10. Percentage of U(VI) species as a function of total U concentration at pH = 5 for the solution modeled in Figure 16. Only species ≥ 0.01% are shown.

The ability to isolate the uranyl-silicato species in solution, and ultimately elucidate its structure, may provide the linkage between speciation in the aqueous phase and the evolution of solid-phase uranyl-silicates. The speciation of uranium in a solution representative of that required for High Energy X-ray Scattering (HEXS) is presented in Figure 17. Both uranium and silicon concentrations are constrained at 0.25 M in perchlorate solution, and $CO_{2(g)}$ is excluded. Due to high initial uranium concentrations, over the modeled pH range uranyl hydrolysis products outcompete uranyl complexation with silica. Even at low pH, dimeric uranyl species are an order of magnitude more concentrated than the uranyl-silicato complex (Table 11).

Aqueous Species	Concentration M	% Total U
UO_2^{++}	2.19E-01	87.48
$(UO_2)_2OH^{+++}$	1.46E-02	5.84
$UO_2H_3SiO_4^{+}$	1.71E-03	0.69
$(UO_2)_2(OH)_2^{++}$	2.16E-04	0.09
UO_2OH^{+}	3.56E-05	0.01

Table 11. Percentage of U(VI) species as a function of total U concentration at pH = 2 for the solution modeled in Figure 17. Only species ≥ 0.01% are shown.

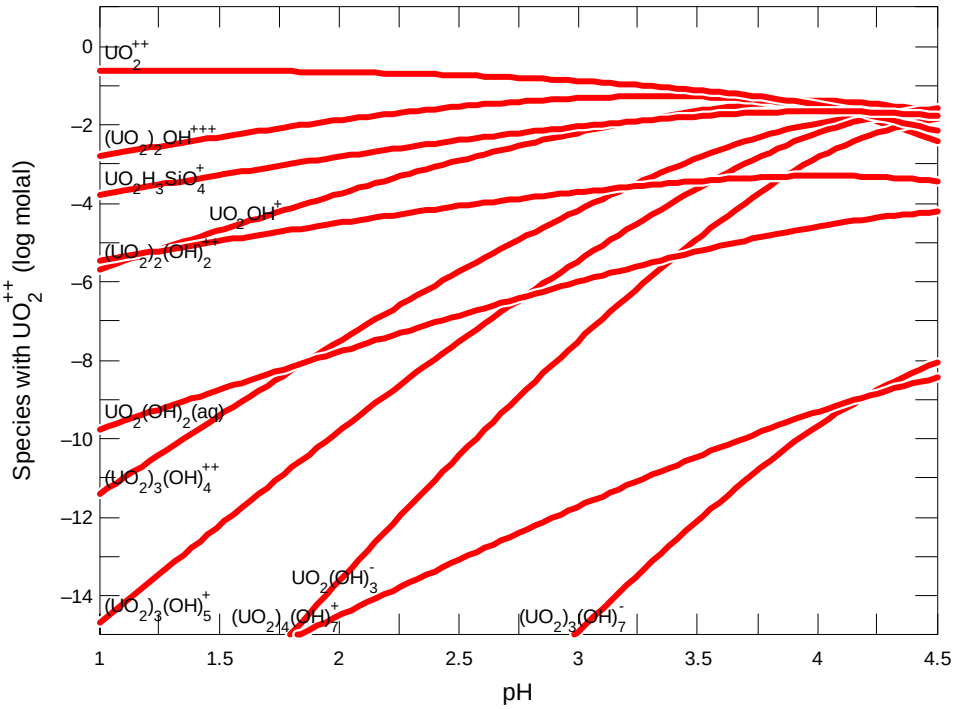

Figure 17. Concentration of U(VI) aqueous species as a function of pH for a 0.25 M U, 0.25 M Si, 0.5 M $NaClO_4$, carbonate-free solution. The $UO_2H_3SiO_4^{+}{}_{(aq)}$ complex was assigned an equilibrium constant as determined by Jensen and Choppin (*3*) as reported in Table 9.

5.2. The Hanford Vadose Zone

At the Hanford Site, overflow from underground storage tank BX-102 discharged 80°C, pH 10, high-level uranium-bearing nuclear waste into vadose zone sediments. The concentrations of uranium and silicon in the tank solution as well as those in contaminated and uncontaminated vadose zone sediments as determined via pore water analysis (*7, 8*) are presented in Table 12. Uranium concentrations decrease from 10^{-1} M in tank solutions to 1.9×10^{-3} M in contaminated pore waters, but remain 10,000 times higher than background levels. The silicon concentration in contaminated pore water, however, is an order of magnitude lower than that of background and tank values, potentially due to the formation uranyl-bearing silicate microprecipitates in fractures of feldspar grains of correlated sediments (*9-12*). As the solubility of amorphous silica increases with pH and temperature it is conceivable that in contaminated vadose zone sediments initial aqueous silicon concentrations may have exceeded that of natural groundwaters (~120 ppm). Raising temperature from 25 to 100°C (at pH 6), or increasing pH from 6 to 10 (at 25°C) enhances silica solubility to ~320, and 310 ppm (1.1×10^{-2} M), respectively (*6*). At 90°C, close to the temperature of the tank solution, silica solubility ranges from ~500-750 ppm (1.8×10^{-2} to 2.7×10^{-2} M) from pH 9 (contaminated pore water) to pH 10 (tank solutions) (*6*). Hence in contaminated pore waters, aqueous silica, derived from dissolving silicate phases, could have exceeded 310 ppm (25°C, pH 9 solution), with the potential for reaching concentrations up to 750 ppm (90°C, pH 10 solution) based on silica solubility alone. At sufficiently high silica concentrations complexation with uranyl may be adequate to induce the precipitation of uranyl-silicate solid phases. Microcrystalline precipitates, as observed in contaminated sediments, may form immediately when uranyl from tank solution and silica from dissolving silicates combine in dilute (uranyl) solution and/or at high temperature (*6*).

	UO_2^{++}	$SiO_{2(aq)}$	pH	T°C
Tank Solution	1.03E-01	4.00E-03	10	80
Contaminated PW	1.85E-03	7.16E-04	9	*
Uncontaminated PW	1.63E-07	4.99E-03	*	*

Table 12. Uranyl and aqueous silica concentrations for solutions relevant to Hanford vadose zone sediments (*7, 8*). The pH of uncontaminated groundwater, though unreported, is likely to be near neutral to mildly basic. Temperatures in sediments may range from ambient (~25°C), for uncontaminated, to close to that of tank solutions for contaminated groundwater immediately below the tank.

PW= Porewater

5.3. Solutions Prepared at UIC (October 2005)

Preliminary experiments were conducted in uranyl nitrate solutions using sodium metasilicate as the silica source. A volume of 0.5 mL 0.46 M $UO_2(NO_3)_2$ stock solution (pH ≈ 1) was added to a 15 mL polypropylene centrifuge tube, and diluted with deionized water such that addition of the appropriate volume of a 0.5 M Na_2SiO_3 stock solution (pH ≈ 14) would produce 1 mL of a 0.01 M Si, 0.25 M U solution. This strategy was undertaken to generate 0.25 M U solutions with Si concentrations ranging from 0.01 to 0.25 M (Table 13). In the case of the 0.25 M Si solution the addition of deionized water was unnecessary to generate the required volume. Solutions were agitated by hand for approximately 1 minute to facilitate mixing, and the final appearance recorded. Immediately following preparation (15-20 minutes), solutions were centrifuged for approximately 20 minutes to ensure separation of any solid phase. A 10 μL aliquot of solution was removed, diluted and prepared for α-counting to determine aqueous U concentrations. This constituted a sample time of approximately 1 hour. The centrifugation and sampling processes were repeated to obtain a 69 hour time point. Initial U concentrations of solutions were determined by analyzing the stock solution and adjusting for dilution. Aqueous-solid phase partitioning of Si was not assessed.

Total Si (M)	Total U (M)	Comments
0.01	0.25	*No visible ppt*
0.05	0.25	*Small quantity of yellow ppt with some gel-like properties*
0.10	0.25	*Increased quantity of yellow ppt (relative to 0.05 M Si)*
0.20	0.25	*Increased quantity of yellow ppt (relative to 0.05 & 0.10 M Si)*
0.25	0.25	*All ppt, bright yellow*

Table 13. Target compositions for experimental solutions and visual appearance subsequent to mixing. The observed mass and intensity of yellow coloration of precipitate increases with initial Si concentration. The remaining solution at 0.25 M Si is virtually colorless.

Experimental results are summarized in Table 14 and Figures 18a and b. Initial Si concentrations in all solutions exceed the solubility of amorphous silica (Figure 18a). Generally speaking, increasing Si results in a decrease in the measured U concentration in solution. An aging effect is only apparent in 0.1 and 0.2 M Si samples, in which aqueous U concentrations at 69 h exceed those of the shorter time-frame—possibly a result of re-release of U to the aqueous phase due to an equilibration process. For initial Si 0.01-0.1 M ~80-90% U remains in solution, with a slight increase in aqueous U as Si is increased. At Si > 0.1 M the most significant loss of U from solution occurs with only ~0-3% remaining in solution.

The ratio of precipitated U to initial Si for all samples is presented in Figure 18b. A decrease in $U_{ppt}/Si_{initial}$ occurs with increasing Si with a minimum at 0.1 M Si and subsequent increase to a value of ~1 at 0.2-0.25 M Si. Assuming that all initial dissolved Si precipitates with uranium for 0.2-0.25 M Si, a solid-phase U:Si ratio of 1 is

commensurate with that of uranophane minerals. Thermodynamically speaking, as Na is present in these solutions, and at sufficiently high concentrations, supersaturation with respect to the uranophane phase Na-boltwoodite is possible (Table 15). In addition, initial Si concentrations ≥ 0.05 M are sufficient to supersaturate the solution with respect to soddyite (U:Si = 2), and in some cases Na-weeksite (U:Si = 2.5) as presented in Table 15. Thermodynamic simulations suggest variation in the composition of the precipitate phase as a function of pH with soddyite dominating at pH ~3-4.5 and Na-boltwoodite becoming significant at pH > 4.5 (Figure 19). At low pH (<3) precipitation of amorphous silica is likely contingent upon initial Si concentration. However, ultimately it is difficult to ascribe a precipitate phase to these samples based on solution composition as the pH of the final solutions was not determined.

	1 h		69 h	
Initial Si (M)	U (M) in soln	$U_{ppt}/Si_{initial}$	U (M) in soln	$U_{ppt}/Si_{initial}$
0.01	0.19	3.77	0.20	3.07
0.05	0.18	0.98	0.18	1.00
0.10	0.21	0.19	0.24	0.00
0.20	0.01	1.11	0.11	0.59
0.25	0.00	0.91	0.00	0.92

Table 14. Concentrations of U in solution and $U_{ppt}/Si_{initial}$ after 1 h and 69 h for initial Si concentrations 0.01-0.25 M. Initial U concentration for all solutions was calculated to be 0.23 M.

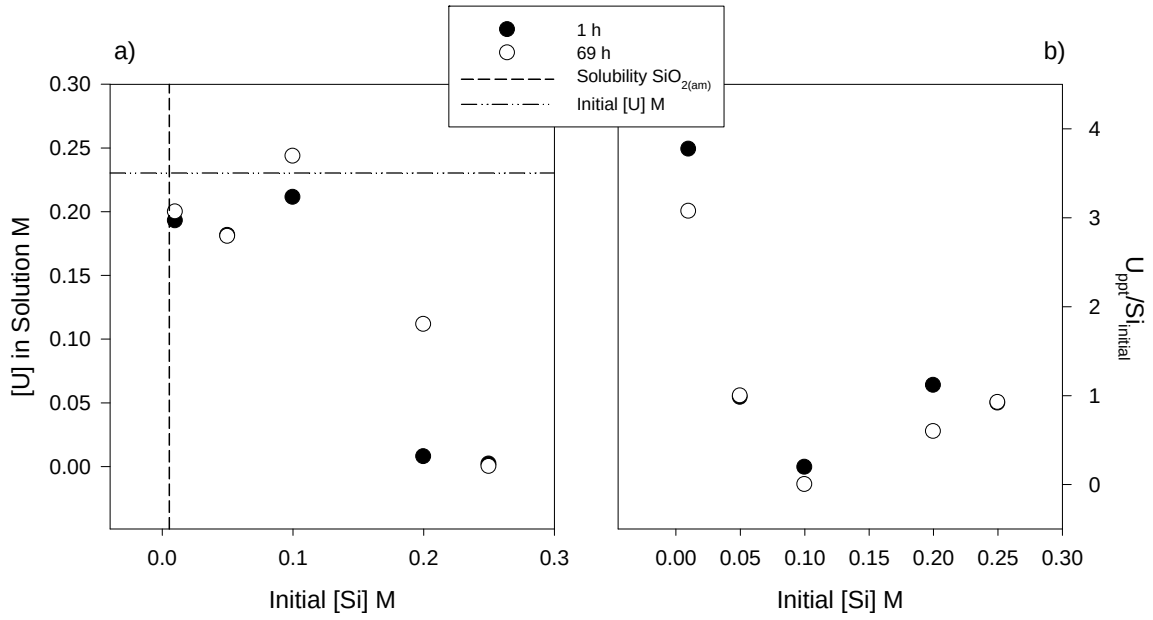

Figure 18a) Aqueous U, and b) the ratio of precipitated U to initial Si as a function of initial Si concentration for 1 h and 69 h reaction times. Initial U = 0.2304 M.

Sample [Si]	1 h; Si req (M)			69 h; Si req (M)		
	Na-Boltwoodite	Soddyite	Na-Weeksite	Na-Boltwoodite	Soddyite	Na-Weeksite
0.01	0.04	0.02	0.09	0.03	0.02	0.08
0.05	0.05	0.02	0.12	0.05	0.02	0.12
0.10	0.02	0.01	0.05	0.00	0.00	0.00
0.20	0.22	0.11	0.56	0.12	0.06	0.30
0.25	0.23	0.11	0.57	0.23	0.12	0.58

Table 15. Molar concentrations of Si, based on precipitated U, required to satisfy U:Si ratios of relevant uranyl silicate minerals. Solutions in which this criterion is met are indicated by shaded boxes.

Na-Boltwoodite: $Na[UO_2(SiO_3OH)](H_2O)_{1.5}$
Soddyite: $(UO_2)_2(SiO_4)(H_2O)_2$
Na-Weeksite: $Na_2(UO_2)_2(Si_5O_{13})\ (H_2O)_3$

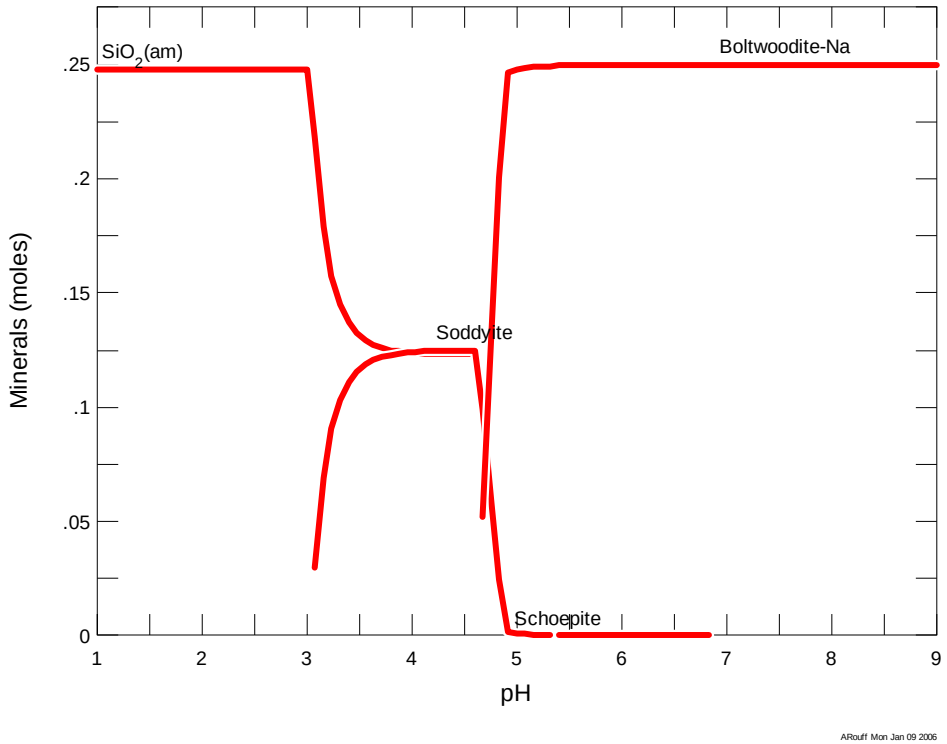

Figure 19. Precipitate phases as a function of pH for a 0.25 M U, 0.25 M Si, 0.5 M $NaNO_3$ background solution in equilibrium with atmospheric $CO_{2(g)}$ ($PCO_{2(g)} = 10^{-3.5}$ atm).

Precipitates of metal silicates usually are difficult to characterize physically as they are often inhomogeneous due to changes in the rate of Si polymerization, and variation in metal to silica ratios during precipitation (*6*). Precipitate composition is not only contingent upon the initial ratio of components (i.e. U and Si) in solution, but upon that of the mixed components—over which there is no control, and likely varies during the precipitation process, resulting in a range of compositions (*6*). So, in addition to the uncertainty in pH and concentrations of precipitated Si, it is difficult to ascribe specific processes to the observed trends. However, any or all of the following are likely here:

(1) Precipitation of amorphous silica induced by a decrease in pH on mixing with U stock solution.
(2) Precipitation of a uranium oxide induced by an increase in pH on addition of silica, or by dilution with water.
(3) Sorption of U to amorphous silica.
(4) Formation of a uranyl-silicate precipitate—potentially Na-boltwoodite or soddyite, with a small chance of Na-Weeksite.
(5) Any combination of the above.

5.4. Solutions Prepared at ANL (October 2005)

All solutions were prepared using a 0.63 M uranyl perchlorate stock solution (pH ≈ 0.4) and either a 0.54 M (Sample Set 1) or 0.13 M (Sample Set 2) sodium metasilicate stock solution (pH not measured). A predetermined volume of $UO_2(ClO_4)_2$ stock was added to a 5 mL glass vial, and Na_2SiO_3 stock added either as a set volume, or in 20-100 μL increments until precipitation was detected visually. The objective using the latter approach was to obtain a sample in which the maximum concentration of Si was added without inducing a precipitate phase. All but solutions 1 & 3 (in Sample Set 1) were stirred. Details for the preparation of all samples are presented in Table 16.

	Sample No.	Volume Si (mL)	Volume U (mL)	Total Volume (mL)	Comments
Sample Set 1	3	0.06	0.82	0.88	*† *pH~1.5*
	1	0.50	0.82	1.33	*5μL $HClO_4$; pH~2.67*
	11	0.47	0.47	0.88	—
Sample Set 2	25	0.25	0.82	1.07	*†
	14	0.50	0.82	1.32	*†
	12	1.00	0.82	1.82	*†
	10	1.20	0.82	2.02	*†
	13	1.35	0.82	2.17	*†
	9	1.50	0.82	2.32	*†
	8	1.80	0.82	2.62	*†

Table 16. Preparation details for Sample Set 1 and 2 solutions. Stock concentrations are reported in the text. The approximate pH of the final solution is reported where measured.

*Si stock added in increments; †Sample stirred

Experimental results are presented in Table 17 and Figure 20. As for solutions prepared at UIC, Si concentrations in all ANL samples exceed the solubility of amorphous silica (Figure 20). Relative to UIC prepared samples (in which initial U concentration is constant at 0.23 M) both U and Si concentrations vary for ANL prepared samples, ranging from 0.20-0.59 M and 0.03-0.29 M, respectively. The general trend for both Sample Set 1 and 2 appears to be an increase in the quantity of visually detectable precipitate with decreasing U and increasing Si concentration. For Sample Set 1 precipitation was evident in all solutions, with a small quantity of precipitate observed at Si concentrations of ~0.04 M (sample 3). This is relatively consistent with results from UIC prepared samples, in which a precipitate was observed at ~0.05 M Si. For samples 3 and 1, using the measured pH, and comparing to thermodynamic solubilities, the likely precipitate phase is amorphous silica (Figure 21). Due to some uncertainty in pH measurements, the potential for some soddyite precipitation in sample 1 cannot be discounted. For Sample Set 2 precipitation was most apparent at Si $\geq$ 0.08 M and U $\leq$ 0.24 M—initial conditions commensurate with those of sample 13. The initial U concentration for this sample is most similar (relative to all other samples, with the exception perhaps of sample 9) to that of UIC prepared samples (0.23 M). The occurrence of precipitation at 0.08 M Si is thus consistent with UIC samples in which precipitates were observed to occur at Si $\geq$ 0.05 M. The processes resulting in clouding or gelling of solutions 13, 9 and 8 on standing is likely to involve those as described above for UIC samples (i.e. points 1 through 5; page 46).

	Sample No.	[Si] M	[U] M	Comments
Sample Set 1	3	0.04	0.59	*Small quantity of ppt*
	1	0.20	0.39	*Significant ppt*
	11	0.29	0.30	*Bright yellow ppt*
Sample Set 2	25	0.03	0.48	*Clear*
	14	0.05	0.39	"
	12	0.07	0.28	"
	10	0.08	0.26	"
	13	0.08	0.24	*Clear, cloudy on stding*
	9	0.08	0.22	*Clear, cloudy on stding*
	8	0.09	0.20	*Cloudy, gel on stding*

Table 17. Initial U and Si concentrations along with the visual appearance of ANL samples subsequent to preparation.

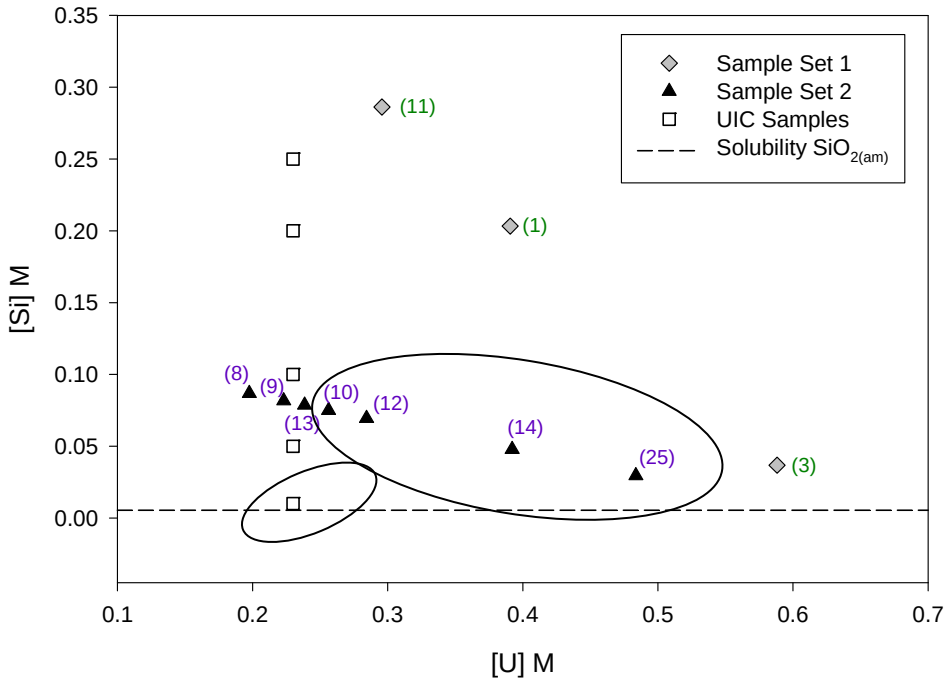

Figure 20. Initial calculated solution compositions for ANL prepared samples. Initial solution compositions for UIC samples are included for comparison. Samples in ovals do not exhibit any observable precipitate phase

a)

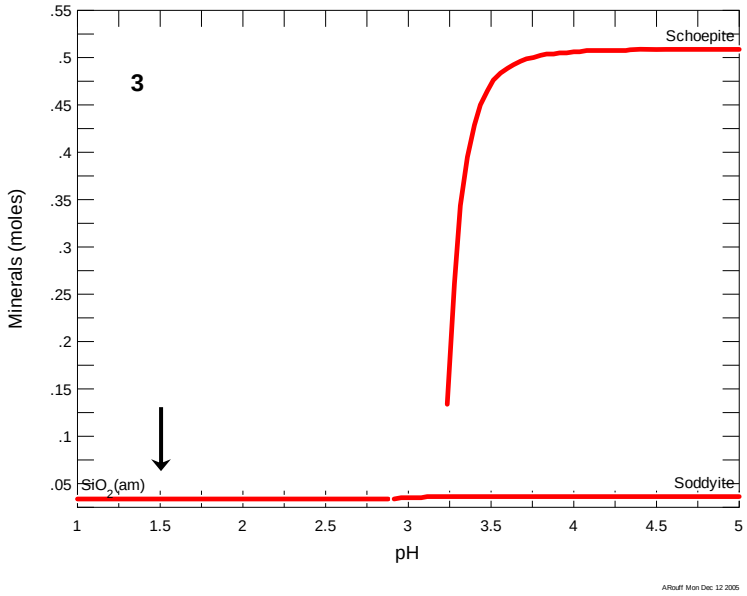

Figure 21a. Precipitate phases as a function of pH for solutions with initial compositions commensurate with those of sample 3. Arrows indicate the measured pH value of the sample.

b)

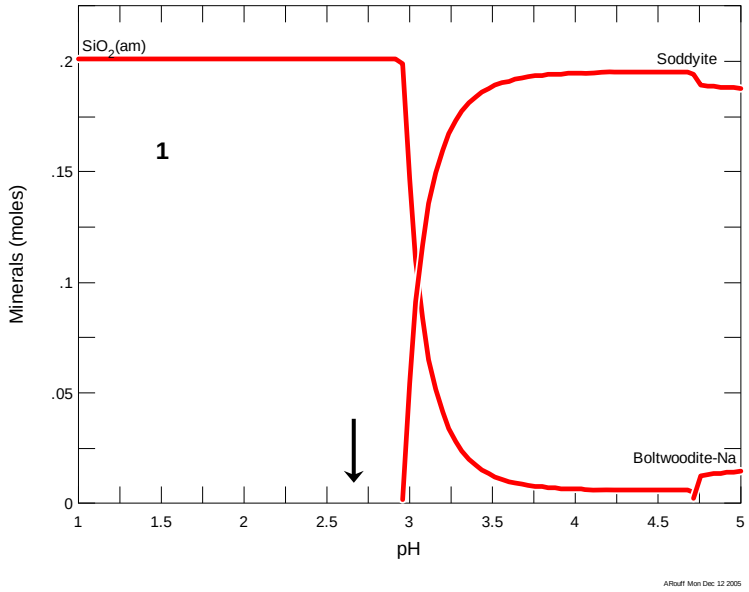

Figure 21b. Precipitate phases as a function of pH for solutions with initial compositions commensurate with those of sample 1. Arrows indicate the measured pH value of the sample.

Though results for ANL samples are relatively comparable to those obtained for UIC samples, there are factors which may contribute to deviation between the two datasets:

(1) Glass vials were used for preparation of ANL samples, thus some sorption of U to glass surfaces may have occurred, resulting in a reduction in actual U concentrations relative to calculated values.

(2) ANL and UIC samples were prepared using a perchlorate and nitrate background, respectively. As U complexation with nitrate is significant in the estimated pH range of the study relative to (inert) perchlorate solutions (Figures 17 and 22) the overall aqueous speciation of U is different. However, the fraction of uranyl complexed as $UO_2H_3SiO_4^+{}_{(aq)}$ appears to remain relatively unaffected (Tables 11 and 18).

(3) ANL samples were prepared via the addition of either concentrated (Sample Set 1) or dilute (Sample Set 2) Si to concentrated U. UIC solutions were prepared via the addition of concentrated Si to dilute or concentrated (0.25 M sample) U. Additionally, for ANL samples, solutions (for the most part) were stirred and Si added incrementally, whilst for UIC samples the entire predetermined volume of Si was added, and shaking but not stirring was implemented. Despite variations in the approach to solution preparation the primary discrepancy between samples appears to be kinetic, in that for ANL samples the precipitation process is delayed as exemplified for samples which appeared to be clear but gelled on standing (Sample Set 2, samples 13, 9 and 8). For the

latter samples, the precipitates formed may exhibit greater homogeneity relative to UIC samples, though this is not guaranteed as the fraction of U bound to Si—and thus the U:Si ratio and composition of the gel—is contingent upon the degree of polymerization (*6*). Hence as gelation proceeds the composition of the precipitate is likely to vary.

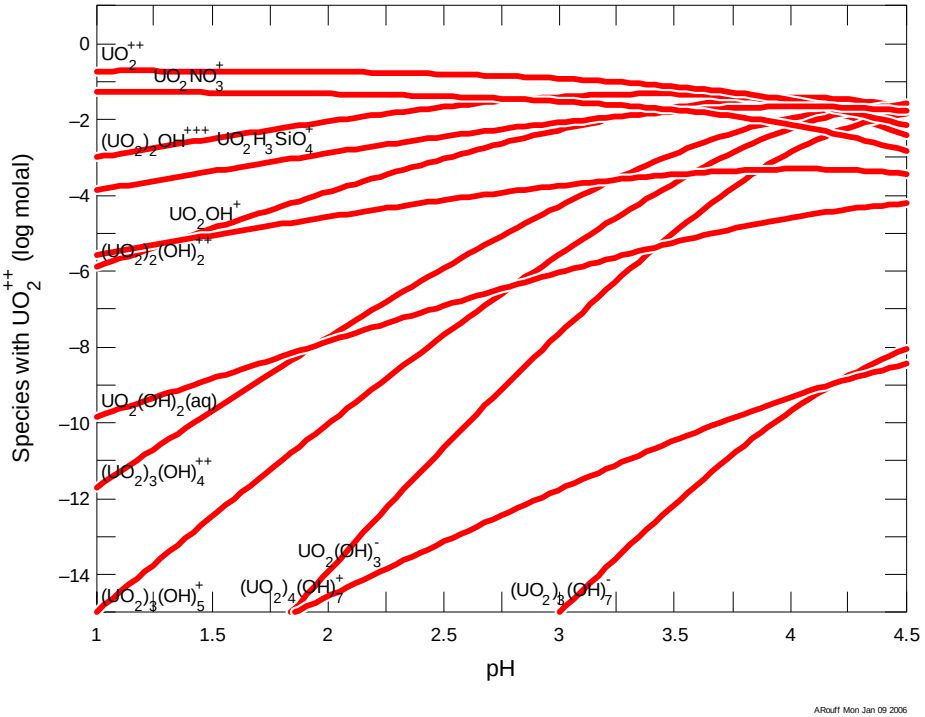

Figure 22. Concentration of U(VI) aqueous species as a function of pH for a 0.25 M U, 0.25 M Si, 0.5 M $NaNO_3$ background, carbonate-free solution. The $UO_2H_3SiO_4^+{}_{(aq)}$ complex was assigned an equilibrium constant as determined by Jensen and Choppin (*3*) as reported in Table 9.

Aqueous Species	Concentration M	% Total U
UO_2^{++}	1.81E-01	72.44
$UO_2NO_3^+$	4.74E-02	18.95
$(UO_2)_2OH^{+++}$	9.92E-03	3.97
$UO_2H_3SiO_4^+$	1.45E-03	0.58
$(UO_2)_2(OH)_2^{++}$	1.51E-04	0.06
UO_2OH^+	3.01E-05	0.01

Table 18. Percentage of U(VI) species as a function of total U concentration at a pH of 2 for the solution modeled in Figure 22. Only species ≥ 0.01% are shown.

5.5. Preliminary spectroscopic results

Tentative results from HEXS experiments, as well as data from potential reference materials (*13-18*) are summarized in Table 19a-b. The pair distribution function (PDF) for the $UO_2(ClO_4)_2$ stock indicates a U-$O_{(ax)}$ distance of ~1.67 Å, which is similar to that observed via X-ray diffraction (*13*) for $UO_2(H_2O)_x^{2+}$, but shorter than typical distances for the aqueous monomer as determined via EXAFS at 1.77-1.81 Å (*14*). Bond lengths of 2.42, 2.88 and 4.52 Å are consistent with U-O_{eq} (*13-16*), O-O_{water} (*19* and references therein) and U-O_{water} (*20*). Results for sample 3 are similar to those of the $UO_2(ClO_4)_2$ stock, likely due to the high U concentration (0.59 M) and low Si concentration (0.04 M) of the sample (Table 9). Both samples 1 and 11 exhibit a peak in the PDF at 3.88-3.90 Å that may be due to U-U scattering as a result of a uranium precipitate phase. Based on Figure 21, this precipitate may be a soddyite phase. A comparison of obtained results with structural data for soddyite (*15*) indicates similarities in U-O_{eq} and U-U distances for both samples relative to soddyite (Table 19). Additionally, the peak at 3.12 Å in sample 11 is similar to that at 3.15 Å for U-Si in soddyite. The presence of this peak at 3.12 Å, as well as the absence of the 2.88 Å O-O_{water} peak in the sample 11 spectrum suggests that this sample is dominated by the solid phase, whereas sample 1 still has a significant aqueous component. This is consistent with the visual appearance of the samples as presented in Table 17. The presence of some minor aqueous phase in sample 11 however is indicated by the persistence of the U-O_{water} peak at 4.51 Å.

a)

	Potential Scattering Paths and Estimated Bond Distances (Å)						
Sample	U-O_{ax}	U-O_{eq}	O-O_{water}	U-Si	U-Si	U-U	U-O_{water}
$UO_2(ClO_4)_2$ stock	1.67	2.42	2.88				4.52
3	1.67	2.42	2.88				4.52
1	1.67	2.42	2.88			3.88	4.52
11	1.69	2.41		3.12		3.90	4.51
10	1.67		2.88		3.81		4.56
13	1.67		2.88		3.81		4.56
9	1.67		2.88		3.81		4.56
8	1.81		2.88		3.81		4.56

Table 19a) Potential scattering paths and estimated bond distances for PDFs of the $UO_2(ClO_4)_2$ stock, all Sample Set 1 (samples 3,1, and 11) solutions, and Sample Set 2 solutions for which data is available (samples 10, 13, 9, and 8).

b)

Reference	Structural Parameters						
$UO_2(H_2O)_x^{2+}$ (*13, 14*)	U-O_{ax}	U-O_{eq}					
N	2	5					
R (Å)	1.70-1.77	2.42					
Soddyite (*15*)	U-O_{ax}	U-O_{eq}	U-O_{eq}	U-O_{eq}	U-Si	U-Si	U-U
N	2	2	1	2	1	2	2
R (Å)	1.78	2.31	2.40	2.42	3.15	3.80	3.86
$(UO_2)_2(OH)_2(H_2O)_6^{2+}$ (*16*)	U-O_{ax}	U-O_{eq}	U-O_{water}	U-U			
R (Å)	1.79	2.36	2.54	3.98			
Amorphous silica (*17, 18*)	U-O_{ax}	U-O_{eq}	U-O_{eq}				
N	2	2	1				
R (Å)	1.78-1.81	2.29	2.50				

Table 19b) Structural parameters for applicable aqueous and solid phase references as reported in the literature.

Spectra for samples 10, 13, 9 and 8 differ from the $UO_2(ClO_4)_2$ stock and all other samples in that a U-O_{eq} distance is not evident, and a peak potentially distinguishable from the U-U (3.88-3.90 Å) peak of samples 1 and 11 becomes apparent at 3.81 Å. As the U concentration is lower in samples 10, 13, 9 and 8 relative to all other solutions, meaning greater dilution, it is plausible that the 2.42 Å U-O_{eq} peak may be masked by the O-O_{water} peak at 2.88 Å, due to low intensity of the former. Due to the cloudy appearance of these samples (gel-like for sample 8) a precipitate phase is present. Thus, the feature at 3.81 Å in the PDF may be due to U-U or U-Si scattering. Based on the structural information for soddyite, U-U scattering occurs at 3.86 Å—a slightly longer distance than that observed in these samples. In addition, peaks that are common to all samples seem to occur at similar distances, suggesting that a soddyite U-U distance for these samples would be consistent with that of samples 1 and 11. Assuming U interactions in the aqueous phase, a U-U distance observed for UO_2^{2+} dimers at 3.98 Å (*16*) seems too large, however, the occurrence of dimerization in these solutions cannot be completely ruled out (e.g. Figure 17 and Table 19). An alternate explanation for this peak may be due to U-Si scattering at 3.81 Å, commensurate with a U-Si distance of 3.80 Å as observed for soddyite (this peak may also be present in sample 1 and 11 spectra, but may be dominated by strong U-U scattering at 3.88-3.90 Å). The apparent absence of U-U backscatterers, and the presence of a peak at 3.80 Å which may be due to U-Si interactions might be indicative of U interaction with a silicate phase such as amorphous silica. Hence, these samples may represent U sorbed to an amorphous silica phase. Also, the U-O_{ax} distance of sample 8 is significantly longer than all other samples at 1.81 Å which is close to that observed for uranyl sorbed to amorphous silica (*18*). As this sample

has the lowest U concentration of all presented samples (Table 9), features as a result of U-Si interactions may be enhanced.

In summary, spectroscopic results thus far suggest (but not conclusively) that several processes may be occurring in these samples. Sample 3 appears to be dominated by $UO_2^{2+}{}_{(aq)}$, while measurable, and significant amounts of probable soddyite precipitate can be detected in samples 1 and 11, respectively. For samples 10, 13, 9 and 8 the obtained spectral parameters may be attributed to sorption of U to an amorphous silica precipitate—this process being most pronounced for sample 8—or small amounts of soddyite precipitate. However, the presence of U dimers cannot be discounted as a contributing factor to the PDFs of sample 10, 13, 9 and 8 solutions.

5.6. Relevance to natural samples

For completeness, initial compositions of both UIC prepared and ANL samples are presented relative to observed U and Si of Hanford site contaminated groundwater and tank solutions (Table 12, Figure 23). Tank and groundwater solutions range in concentration from 10^{-1} to 10^{-3} M U, and 10^{-4} to 10^{-3} Si. Experimental solutions are twice as concentrated in U relative to tank solutions, and up to two orders of magnitude more concentrated than groundwater solutions. Also, Si concentrations in experimental solutions are one to two orders of magnitude greater than those of tank and groundwater solutions. In addition, as carbonate (and phosphate) concentrations are high in both environmental solutions, a significant portion of U(VI) is complexed with this moiety. This, combined with high pH, and potentially higher temperature of tank and groundwater solutions, as discussed in Section 5.2, results in notable differences in the aqueous speciation of U(VI) in these relative to experimental solutions. Hence, processes as observed in experimental solutions may not necessarily be applicable to those of the Hanford vadose zone. However, due to the inherent complexity of environmental samples the approach taken thus far, and procedures proposed in the following section, may provide simplified, but fundamental answers to U(VI) complexation, polymerization, and ultimately precipitation, with silicate species.

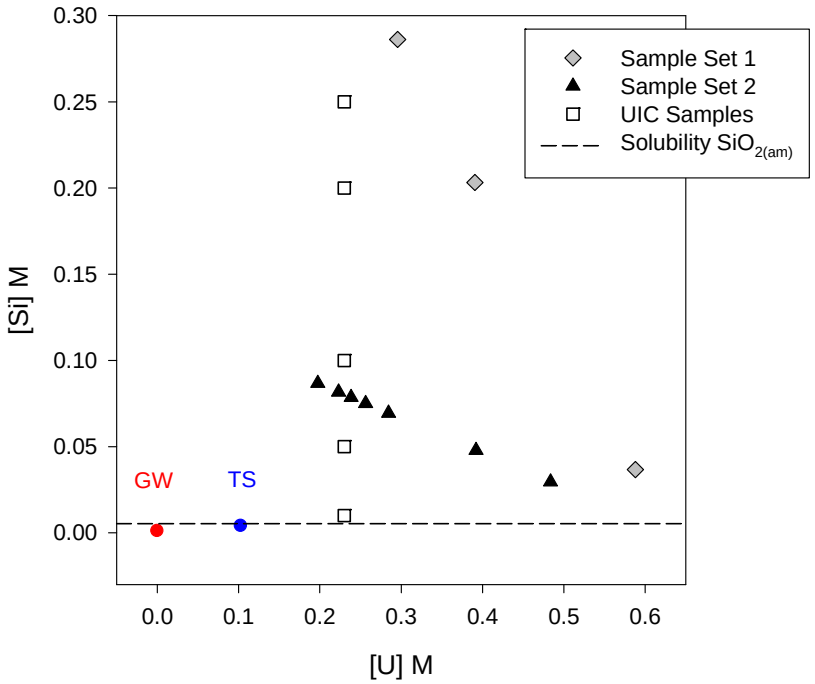

Figure 23. Initial U and Si of UIC and ANL samples (HEXS compatible) with that of actual Tank and Groundwater solutions.

GW = Contaminated groundwater; TS = Tank Solution

5.7. References

(1) Porter R.A. and Weber W.J. (1971) The interaction of silicic acid with iron(III) and uranyl ions in dilute aqueous solution. *Journal of Inorganic and Nuclear Chemistry*. **33**, 2443-2449.

(2) Satoh I. and Choppin G.R. (1992) Interaction of uranyl(VI) with silicic-acid. *Radiochimica Acta*. **56**, 85-87.

(3) Jensen M.P. and Choppin G.R. (1998) Complexation of uranyl(VI) by aqueous orthosilicic acid. *Radiochimica Acta*. **82**, 83-88.

(4) Moll H., Geipel V., Brendler G., Bernhard H. and Nitsche H. (1998) Interaction of uranium(VI) with silicic acid in aqueous solutions studied by time-resolved laser-induced fluorescence spectroscopy (TRLFS). *Journal of Alloys and Compounds*. **271–273**, 765–768.

(5) Hrnecek E. and Irlweck K. (1999) Formation of uranium(VI) complexes with monomeric and polymeric species of silicic acid**.** *Radiochimica Acta*. **87**, 29-35.

(6) Iler R.K. (1979) *The chemistry of silica: Solubility, polymerization, colloid and surface properties, and biochemistry*. John Wiley & Sons Inc., New York. 866 p.

(7) Lichtner P. C. (2002) Simulated B, BX, BY tank farms supernate composition. *Field Investigation Report for Waste Management Area B-BX-BY*. v. 2, RPP-10098, CH2M HILL Hanford Group, Inc., Richland, Washington.

(8) Serne R. J., Last G. V., Gee G. W., Schaef H. T., Lanigan D. C., Lindenmeier C. W., Lindberg M. J., Clayton R. E., LeGore V. L., Orr R. D., Kutnyakov I. V., Baum S. R., Geiszler K. N., Brown C. F., Valenta M. M. and Vickerman T. S., (2002) *Characterization of Vadose Zone Sediment: Borehole 299-E33-45 Near BX-102 in the B-BX-BY Waste Management Area*, PNNL-14083, Draft, Pacific Northwest National Laboratory, Richland, Washington.

(9) McKinley J. P., Heald S. M., Zachara J. M., and Resch C. (2002) The Identification of Uranium-Bearing Phases By X-Ray Microprobe, Electron Microprobe, and Scanning Electron Microscopy. *Field Investigation Report for Waste Management Area B-BX-BY.* v. 2, RPP-10098, CH2M HILL Hanford Group, Inc., Richland, Washington.

(10) Catalano J. G., Heald S. M., Zachara J. M., and Brown G. E. Jr. (2004) Spectroscopic and diffraction study of uranium speciation in contaminated vadose zone sediments from the Hanford Site, Washington State. *Environmental Science & Technology*. **38**, 2822-2828.

(11) Wang Z., Zachara J. M., Gassman P. L., Liu C., Qafoku O., Yantasee W. and Catalano J. G. (2005) Fluorescence spectroscopy of U(VI)-silicates and U(VI)-contaminated Hanford sediment. *Geochimica et Cosmochimica Acta*. **69**, 1391-1403.

(12) Liu C., Zachara J. M., Qafoku O., McKinley J. P., Heald S. M., and Wang Z. (2004) Dissolution of uranyl microprecipitates in subsurface sediments at Hanford Site, USA. *Geochimica et Cosmochimica Acta*. **68**, 4519-4537.

(13) Åberg M., Ferri D., Glaser J., and Grenthe I. (1983) Structure of the hydrated dioxouranium(V1) ion in aqueous Solution. An X-ray diffraction and ^{1}H NMR study. *Inorganic Chemistry.* **22,** 3986-3989.

(14) Thompson H.A., Brown G.E., and Parks G.A. (1997) XAFS spectroscopic study of uranyl coordination in solids and aqueous solution. *American Mineralogist.* **82**, 483-496.

(15) Demartin F., Gramaccioli C.M., and Pilati, T. (1992) The importance of accurate crystal structure determination of uranium minerals: II. Soddyite. *Acta Crystallographica.* **C48**, 1–4.

(16) Tsushima S., and Reich T. (2001) A theoretical study of uranyl hydroxide monomeric and dimeric complexes. *Chemical Physical Letters*. **347**, 127-132.

(17) Dent A.J., Ramsay J.D.F., and Swanton S.W. (1992) An EXAFS study of uranyl-ion in solution and sorbed onto silica and montmorillonite clay colloids. *Journal of Colloid and Interface Science*. **150**, 45-60.

(18) Reich T., Moll H., Denecke M.A., Geipel G., Bernhard G., Nitsche H., Allen P.G., Bucher J.J., Kaltsoyannis N., Edelstein N.M., and Shuh D.K. (1996) Characterization of hydrous uranyl silicate by EXAFS. *Radiochimica Acta*. **74**, 219-223.

(19) Xenides D., Randolf B.R., and Rode B.M. (2006) Hydrogen bonding in liquid water: An ab initio QM/MM MD simulation study. *Journal of Molecular Liquids*. **123**, 61-67.

(20) Soderholm L., Skanthakumar S., and Neuefeind J. (2005) Determination of actinide speciation in solution using high-energy x-ray scattering. *Analytical and Bioanalytical Chemistry*. **383**, 48-55.